Control of Wakes and Vortex-Induced Vibrations of a Single Circular Cylinder Using Synthetic Jets

Chenglei Wang[1], Hui Tang[2,*], Fei Duan[1], Simon C. M. Yu[3]

[1]School of Mechanical & Aerospace Engineering, Nanyang Technological University, Singapore 639798

[2]Department of Mechanical Engineering, The Hong Kong Polytechnic University, Kowloon, Hong Kong SAR, China

[3] Singapore Institute of Technology, Singapore 179104

[*] Corresponding author: h.tang@polyu.edu.hk

Abstract: This paper presents a study on active control of the wakes and one-dimensional vortex-induced vibrations (VIVs) of a single circular cylinder using a pair of synthetic jets (SJs) at a low Reynolds number Re = 100. To facilitate this study, a lattice Boltzmann method based numerical framework is established, in which the multi-block scheme and the overlap-mesh approach with improved information exchange mechanisms are used to balance the computational accuracy and efficiency, and the interpolated bounce-back scheme and a corrected momentum exchange scheme are adopted for accurate force evaluation. Two configurations are considered. In the first configuration, the cylinder is fixed, on which a pair of SJs is implemented and operates in phase. Effects of the SJ pair on the cylinder wake are investigated in a systematical way, with the focus placed on the SJ's momentum coefficient, frequency and position. Simulation results indicate that the Kármán vortex street formed behind the cylinder can be effectively suppressed when the SJ pair operates with sufficiently high momentum coefficient, at a frequency close to the cylinder's natural vortex shedding frequency, and is placed in the quarter arc edge of the cylinder's leeward side. In the second configuration, the same cylinder is allowed to oscillate in the cross-flow direction under the excitation of asymmetrically shedding vortices as well as the constraint of a spring. It is well demonstrated that this one-dimensional VIV of the cylinder can be successfully suppressed by the use of SJ control.

Due to stronger vortex shedding induced by increased relative motion between the cylinder and its surrounding flow, however, not all the cases that perform complete wake suppression on the fixed cylinder are able to completely suppress the VIVs of the oscillating cylinder. Through the present study, details about SJ-controlled flow around the cylinder and in the wake are also revealed.

Keywords: Synthetic Jet, Wake Control, Vortex-Induced-Vibration Control, Lattice Boltzmann Method.

1. Introduction

Asymmetric vortices shed from bluff structures in flows cause dynamic loading on the structures. When the shedding frequency matches the structure's natural frequency, large-amplitude vibrations may occur, and, if that happens, the structure is prone to damage due to extreme stress or fatigue. Therefore, it is desirable to control the asymmetric vortex shedding and suppress the vortex-induced vibrations (VIVs). For years, numerous flow control methods have been used to suppress the asymmetric vortex shedding and VIVs, including passive (no power required), active open-loop (no sensor required) and active closed-loop (sensor required) schemes, on which Choi et al. (2008) has given a comprehensive review.

As a promising active flow control method, synthetic jets (SJs) have been used in various applications, including flow separation control (Wang et al. 2007; Tang et al. 2014), mixing control (Pavlova et al. 2008), and turbulence control (Rathnasingham and Breuer 2003). A SJ is a chain of vortex rings/pairs produced through a small orifice/slot by oscillation of single or multiple diaphragms attached to a cavity. An attractive feature of the SJ is that it can produce non-zero momentum flux to control ambient flows with zero net mass flux. Since its emergence, the SJ technology has been applied on bluff bodies to modify wakes and control VIVs. Using a single SJ, Feng et al. (2010) and Feng and Wang (2012, 2014b) experimentally investigated its effects on wake modification and drag reduction of a cylinder. The same group (Feng and Wang, 2010, 2014a) also investigated the effects of a

single SJ on modifying wakes when the SJ is located at the rear or front stagnation point of a cylinder. For control using multiple SJs, Williams et al. (1992) utilized a pair of in-phase and out-of-phase SJs operating at low frequencies to alter vortex shedding frequencies and wake patterns behind a cylinder at a cylinder diameter based Reynolds number Re = 470. Munday and Taira (2013) investigated the effects of excitation frequency and velocity amplitude of a pair of out-of-phase SJs on the lock-on characteristics and drag reduction of a cylinder at Re = 100. And Ma et al. (2014) found several new wake patterns behind a circular cylinder, such as the symmetric 2P mode and asymmetric 2P+2S mode, when a pair of in-phase SJs is implemented. In addition to on circular cylinders, SJs were also applied on bluff bodies of other shapes. Pastoor et al. (2008) employed a pair of SJs on a D-shape cylinder for the purpose of drag reduction. By applying a feedback controller, they experimentally achieved a 15% drag reduction at the body height based Reynolds number ranging from 23,000 to 70,000. They attributed the drag reduction to the mechanism that the use of in-phase SJs enhances the initial symmetry of the wake by forcing synchronous vortex shedding. Parkin et al. (2014) did a numerical study on a similar D-shape cylinder. At the Reynolds number of 23,000, they found the optimal drag reduction occurred at the SJ forcing frequency approximately half of the natural vortex shedding frequency.

Although in some of the above-mentioned investigations SJs have been applied to modify wakes of single circular cylinders, their effects at very low Reynolds numbers such as Re = O(100) have not been fully understood, and the control was mainly focused on drag reduction instead of VIV mitigation. The VIV control at such low Reynolds numbers is still meaningful and worth investigating. For instance, the VIVs of a hot-wire or hot-film probe may cause significant errors in the velocity or temperature measurements (Perry and Morrison 1971; Atta and Gharib 1987; Anderson et al. 2005). Although its practical implementation is very challenging, the SJ control can be a new way of handling similar low-Reynolds-number VIV problems. Therefore, the present study aims to investigate the effects of three key parameters of a pair of SJs, i.e., the momentum coefficient, frequency, and location, on suppressing the asymmetric vortex shedding and one-dimensional VIVs of a circular cylinder at a Reynolds number Re = 100. To focus the present investigation, this

pair of SJs is placed symmetrically about the cylinder's centerline, issues along the incoming flow direction, and operates in phase.

This paper is organized as follows. In Section 2 two SJ-based flow control problems are described. In Section 3 a lattice Boltzmann method based numerical framework is introduced and validated. Section 4 presents the results and discussions associated with the two simulation scenarios. In the end conclusions from the present study are drawn.

2. Problem description

In the present study, two SJ-based flow control problems are considered: control of asymmetric wakes behind a fixed circular cylinder and the resulting lift oscillation experienced by the cylinder, and control of one-dimensional VIVs of the same cylinder that is allowed to move in the cross-flow direction. In both problems, the diameter-based Reynolds number is fixed at Re = 100, at which the flow is unsteady, laminar and two dimensional as reported by Williamson (1996).

2.1. Fixed cylinder in uniform flows

In this problem, a circular cylinder is horizontally immersed in a uniform flow. At the Reynolds number of interest, i.e., Re = 100, the flow around the cylinder will be governed by absolute wake instability. The upper and lower shear layers will strongly interact, as depicted in Fig. 5a. The vortex A that is produced by the roll-up of the upper shear layer pulls the lower shear layer up and hence induces the creation of the new vortex B. Once growing and convecting downstream, vortex B will trigger the creation of a new vortex from the upper shear layer. In this way, strong vortices of opposite signs shed and convect alternatively in the wake, forming a von Kármán vortex street. To control this asymmetric wake and the resulting lift oscillation experienced by the cylinder, a pair of SJs is implemented on the leeward portion of the cylinder, symmetrical about the cylinder's horizontal centerline, as shown in Fig. 1.

The SJs are activated after the flow achieves its steady state. Their velocity is given as

$$\boldsymbol{u}_{sj}^{u} = U_{\max} \sin\left(2\pi f_e t + \phi_u\right)\left(\cos\left(\beta\right), \sin\left(\beta\right)\right) \tag{1}$$

$$\boldsymbol{u}_{sj}^{l} = U_{\max} \sin\left(2\pi f_e t + \phi_l\right)\left(\cos\left(-\beta\right), \sin\left(-\beta\right)\right) \tag{2}$$

where the superscripts "*u*" and "*l*" indicate the upper and lower SJs, respectively. $U_{\max}$ is the amplitude of jet velocity, f_e the excitation frequency, ϕ_u and ϕ_l the operating phases of the two SJs, and β the SJ orientation angle defined relative to the cylinder's horizontal centerline. A non-dimensional SJ excitation frequency is defined as

$$f^* = \frac{f_e}{f_n} \tag{3}$$

where f_n is the natural frequency of vortex shedding from the cylinder. The momentum coefficient of the SJ pair characterizes the SJ strength and is defined as

$$C_\mu = \frac{2{U_{\max}}^2 d}{{U_\infty}^2 D} \tag{4}$$

where d is the width of SJ actuators and U_∞ the incoming flow velocity. In the present study, this width is set as 1/72 of the cylinder perimeter, i.e., $d = \pi D/72$.

Fig. 1 and Eqs. (1) to (4) reveal that the SJ performance depends on five non-dimensional parameters, i.e., the momentum coefficient C_μ, operating frequency f^*, position angle γ, orientation angle β and phase angle ϕ.

2.2. Oscillating cylinder in uniform flows

In this problem, the cylinder geometry, incoming flow condition, and SJ operation condition are exactly the same as in the previous problem. The only difference is that the cylinder is now connected to a spring-damper system and hence is allowed to move in the cross-flow direction, as depicted in Fig. 2. The SJs are activated when the cylinder transversely oscillates in the steady state, so as to damp the one-dimensional VIV of the cylinder.

The dynamics of the oscillating cylinder is governed by

$$m\ddot{y} + C\dot{y} + Ky = F_L(t) \tag{5}$$

where m is the mass of the cylinder, C the damping factor, K the spring stiffness and F_L the time-dependent lift force experienced by the cylinder. Define two dimensionless variables

$$\tilde{y} = \frac{y}{D}$$

$$\tilde{t} = \frac{tU_\infty}{D}$$

The dimensionless governing equation for the oscillating cylinder can be expressed as

$$\frac{d^2\tilde{y}}{d\tilde{t}^2} + \left(\frac{4\pi\zeta_s}{U_R}\right)\frac{d\tilde{y}}{d\tilde{t}} + \left(\frac{4\pi^2}{U_R^2}\right)\tilde{y} = \frac{C_L}{2m^*} \tag{6}$$

where C_L is the time-dependent lift coefficient, defined as

$$C_L = \frac{2F_L}{\rho_0 U_\infty^2 D} \tag{7}$$

ρ_0 is the mean fluid density. In Eq. (6) m^* is the mass ratio defined as

$$m^* = \frac{m}{\rho_0 D^2} \tag{8}$$

ζ_s is the non-dimensional damping coefficient

$$\zeta_s = \frac{C}{2\sqrt{Km}} \tag{9}$$

and U_R is the reduced velocity defined as

$$U_R = \frac{U_\infty}{f_N D} \tag{10}$$

where f_N is the natural frequency of the present mass-spring-damper system in vacuum

$$f_N = \frac{1}{2\pi}\sqrt{\frac{K}{m}} \tag{11}$$

Since the purpose of Problem 2 is to demonstrate the capability of SJs in controlling the one-dimensional VIV of the cylinder, only one selected set of cases is investigated in the present study, i.e., m^* = 2, U_R = 5 and ζ_s = 0. Under this set of conditions, the SJ pair operates in exactly the same way as for the fixed cylinder in Problem 1.

2.3. Case summary

To focus the analysis, the present study only investigates the effects of three major SJ parameters, i.e., the momentum coefficient C_μ, operating frequency f^* and position angle γ, on the lift experienced by the fixed cylinder and its wake patterns. The values of these parameters are selected in such a way that different control effects can be observed. Five C_μ values, three f^* values, and five γ values are selected, which are listed in Table 1. Therefore in total 75 cases are simulated. In all the cases, the SJ orientation angle, β, is fixed at 0°, meaning that the SJs are always issued horizontally regardless their location. In addition, the two SJs are operated in phase, i.e., ϕ_u - ϕ_l = 0. The two SJs are switched on at the instant when the steady-state lift experienced by the cylinder reaches zero from negative values.

Note the three selected frequencies are all greater than 1. This is because, during the process of selecting the frequency values, it was found that, in addition to the suppression of asymmetric vortex shedding, the SJs operating at around f^* = 1 also induce another very interesting phenomenon, i.e., lock-on of the wake to the actuation frequency (Munday and Taira 2013). To focus the discussions only on the suppression of wake asymmetry and VIVs, therefore, the frequencies around 1 are intentionally skipped in the present study and will be specifically investigated in our next work. Furthermore, the three selected frequencies increase exponentially from 5 to 125, such that two SJ operating modes, i.e., the synthetic jet mode and the acoustic mode, can be covered, which will be revealed in details in later sections.

Obtained from the time-averaged velocity field simulated by Munday and Taira (2013), the mean separation point on the cylinder at the same Reynolds number (Re = 100) is at about γ = 58°. Therefore the selected locations γ = 10°/30°/50° are downstream, and γ = 70°/80° are upstream of the separation point.

As for the control of the oscillating cylinder, the same 75 cases are simulated. For the

purpose of demonstrating the SJ effectiveness in VIV control, however, the results from just one case with C_μ = 2.149, f^* = 5, and γ = 30° is presented in this paper.

3. Numerical method

3.1. Lattice Boltzmann method

To obtain the instantaneous flow field around and behind the cylinder in the two problems described in Section 2, the lattice Boltzmann method (LBM) is adopted, which is effective and efficient in solving complex fluid flows using microscopic models and mesoscopic kinetic equations (Chen and Doolen, 1998). The present simulations use the incompressible D2Q9 MRT LBE model, i.e., two-dimensional incompressible multiple-relaxation-time lattice Boltzmann equation model with nine discrete velocities. Compared to the conventional D2Q9 LBE model, the use of MRT technique can achieve improved numerical stability and accuracy as pointed out by Lallemand and Luo (2000) and Ginzburg and d'Humières (2003). In this model, the computational domain is discretized into a number of square lattices and fluid particles are represented by distribution functions f_α, where α indicates the particle moving direction. The redistribution and propagation of fluid particles are accomplished through a two-step, collision-streaming process. More details about the LBE model can be found in Lallemand and Luo (2000).

3.2. Computational geometry and mesh

Fig. 3 shows the computational domain used in the present study. A uniform flow flows from the left to the right with a speed U_∞ in a 60D (L) × 20D (W) channel. The circular cylinder, fixed or movable, is initially placed in the centerline of the channel. Its center is set 20D downstream from the channel inlet, which has been proved adequate by Jiang et al. (2013). The top and bottom boundaries represent the two channel walls. Instead of being stationary, these two wall boundaries are set moving together with the incoming flow, so that a uniform flow in an infinite domain around the cylinder is simulated, and meanwhile the computational time is significantly saved. Note that the chosen channel

width 20D is a bit smaller than those usually used in literature and also smaller than in the validation cases (see Section 3.6). This choice is based on the consideration on the required computational time and storage space for a large number of cases. Although this narrower channel width does affect the wake and aerodynamic forces as revealed in Section 4.1, it will not affect the analysis as long as it remains the same for all the investigated cases.

To enhance the computational efficiency while maintaining sound accuracy, the MRT multi-block scheme proposed by Yu (2002) is applied in the present study. As shown in Fig. 3, the entire computational domain is divided into four sets of blocks with the mesh density being increased by a factor of 2. The mesh density gradually increases with the increase of block number. That is, Block 4 that contains the cylinder has the finest mesh spacing $\Delta x = D/60$, and Blocks 1.1 to 1.4 that are farthest from the cylinder have the coarsest mesh spacing $8\Delta x$.

Furthermore, for accurate and efficient evaluation of the aerodynamic forces on the cylinder, an overlap mesh is applied, initially overlapping the mesh in Block 4 and then moving together with the cylinder as time advances. This overlap mesh is realized using the arbitrary Lagrangian-Eulerian (ALE) approach (Meldi et al., 2013), but with two improvements incorporated. First, it is the distribution function f_α instead of macroscopic variables such as velocity and pressure that are transferred between the overlap mesh and the fixed mesh. This avoids unnecessary variable conversion and hence improves numerical accuracy. Second, given the fact that during each time step the flow information on one node can only be streamed to its neighboring nodes, in the present approach the information exchange between the overlap mesh and the fixed mesh at each time step occurs in only three rows/columns of grids that cover the interfaces of the two sets of meshes. Compared to the process used in Meldi et al. (2013) where the information of the entire overlap mesh is transferred, the present method can save significant computational costs without degrading the numerical accuracy.

3.3. Boundary and initial conditions

The boundary conditions are also shown in Fig. 3. At the channel inlet, the non-reflecting inlet boundary condition proposed by Izquierdo and Fueyo (2008) is used, whereas at the channel outlet, the homogenous Neumann boundary condition is implemented. On the top and bottom walls, the Dirichlet boundary condition is applied with the x-component velocity U_∞ and y-component velocity 0.

The SJ actuators are represented by a number of nodes on the cylinder, and the time-dependent SJ velocities are realized by enforcing $\boldsymbol{u}_{sj}^{u}$ and $\boldsymbol{u}_{sj}^{l}$ on these nodes. Therefore, the velocity boundary condition representing the SJ actuators on the fixed cylinder is

$$\boldsymbol{u}_w^{sj} = \begin{cases} \boldsymbol{u}_{sj}^{u} & \boldsymbol{r}_w \in \partial\Omega_{sj}^{u} \\ \boldsymbol{u}_{sj}^{l} & \boldsymbol{r}_w \in \partial\Omega_{sj}^{l} \end{cases} \tag{12}$$

where $\boldsymbol{r}_w$ is the position vector of a node, and $\partial\Omega_{sj}^{u}$ and $\partial\Omega_{sj}^{l}$ are the portions on the cylinder representing the upper and lower SJ actuators, respectively. For the moving cylinder, the velocity on the entire cylinder wall is the superposition of the SJ velocity $\boldsymbol{u}_w^{sj}$ and the translational velocity $\boldsymbol{u}_w^{cm}$ of the cylinder

$$\boldsymbol{u}_w = \boldsymbol{u}_w^{cm} + \boldsymbol{u}_w^{sj} \quad \boldsymbol{r}_w \in \partial\Omega_c \tag{13}$$

where $\partial\Omega_c$ represents the cylinder surface.

To evaluate the change of flow when it encounters the fixed or oscillating circular cylinder, the interpolated bounce back scheme proposed by Lallemand and Luo (2003) is applied to adjust the distribution function near the cylinder after each collision/streaming process. By applying the second-order interpolation, this scheme outperforms its ancestor, i.e., the standard half way bounce back scheme.

The velocity of the uniform incoming flow is set as U_∞/c = 0.01, where c is the lattice velocity. Since $D = 60\Delta x$, the non-dimensional time step is Δt = 1/6000, much smaller than Δt = 1/1200 that is used in Jiang et al. (2013) at the same Reynolds number.

3.4. Force evaluation

For fluid-structure interaction problems involving passively moving bodies such as in Problem 2, accurate evaluation of aerodynamic forces on the cylinder and hence the cylinder's motion is of vital importance. To achieve this, a corrected momentum exchange scheme that incorporates the initial momentum of net mass transfer proposed by Chen et al. (2013) is adopted in the present study.

3.5. Vortex tracking method

To quantify the SJ effects on the vortex generation and evolution, an algorithm that identifies and tracks vortex cores is developed and integrated into the numerical framework. The definitions of relevant vortex parameters follow those used by Jardin and Bury (2012). The non-dimensional vorticity ω^* is defined as

$$\omega^* = \frac{\omega D}{U_\infty} \tag{14}$$

where ω is vorticity. The non-dimensional vortex circulation Γ^* is defined as

$$\Gamma^* = \frac{\Gamma}{DU_\infty} = \frac{\iint_\Sigma \omega dxdy}{DU_\infty} \tag{15}$$

where Σ encloses the vortex core region identified using the λ_{ci} criterion (Zhou et al., 1999). The non-dimensional location of the vortex centroid (x_c^*, y_c^*) is evaluated by

$$x_c^* = \frac{x_c}{D} = \frac{\iint_\Sigma x\omega dxdy}{D\Gamma} \tag{16}$$

$$y_c^* = \frac{y_c}{D} = \frac{\iint_\Sigma y\omega dxdy}{D\Gamma} \tag{17}$$

3.6. Validation

The present numerical framework is validated through two case studies. One is the simulation of flow around a fixed cylinder at Re = 100. In this case, the cylinder is located along the centerline of a channel of 60D length and 40D width, and 20D

downstream from the inlet. The diameter of the cylinder is set as $D = 48\Delta x$. The uniform incoming velocity is set as $U_\infty/c = 0.01$.

The flow is inherently unsteady at Re = 100. The oscillation magnitude of the lift coefficient $|C_L|$ and the Strouhal number St are listed and compared with experimental and simulation results obtained from other researchers in Table 2, where the Strouhal number is defined as

$$St = \frac{f_n D}{U_\infty} \tag{18}$$

It can be seen that the present numerical results agree well with the previous results: the St value matches the experimental data and is only 1.2% higher than the values obtained from the Navier-Stokes solvers, and the $|C_L|$ value falls between the other two simulation results with a mean discrepancy of 3.6%.

In the second case, the cylinder is allowed to move in the cross-flow direction at Re = 150, under the constraint of a spring, hence the dynamics of the cylinder is governed by Eq. (6). The mass ratio m^* is set as 2, the damping coefficient ζ_s is set as 0, and the reduced velocity U_R varies from 3 to 8 with an increment of 1. This VIV problem has been well studied by Ahn and Kallinderis (2006) using the finite volume ALE scheme, by Borazjani et al. (2008) using the curvilinear immersed boundary method, and by Jiang et al. (2013) using the LBM.

Dimensions of the computational domain for this validation case are set identical to those used in Jiang et al. (2013), where the cylinder is located along the centerline of a channel with 48D length and 24D width, and 12D downstream from the inlet. The diameter of the cylinder is set as $D = 48\Delta x$. The uniform freestream velocity is also set as $U_\infty/c = 0.01$.

Fig. 4 compares the simulated non-dimensional oscillation amplitude $A^* = A_{\max}/D$ of the cylinder with those obtained from references at various reduced velocity U_R. It is found that the present simulation results are reasonably close to with Jiang et al. (2013)'s

results, with a mean discrepancy of 3.9%. However, relatively larger discrepancies are observed if compared with the results reported by Ahn and Kallinderis (2006) (mean difference of 5.9%) and Borazjani et al. (2008) (mean difference of 9.0%). The reason for these discrepancies may stem from the use of different numerical solvers and curved boundary treatment methods.

4. Results and discussions

The simulation results are reported and discussed in this section. The results of the uncontrolled fixed and vibrating cylinder cases are presented first to serve as the benchmark. Then the effects of three SJ parameters, i.e., the momentum coefficient, frequency, and location, on the lift force experienced by the fixed cylinder and its wake pattern are discussed. In the end, the same set of SJ control cases on the vibrating cylinder is simulated to investigate the capability of SJs in suppressing the one-dimensional VIV of the cylinder.

4.1. Uncontrolled flow

The two steady-state wake patterns behind the uncontrolled fixed and vibrating cylinders are shown in Fig. 5, where the solid and dash lines represent isolines of λ_{ci} = 0.2 that enclose vortex cores of positive and negative vorticity, respectively. Although these two wake patterns seem very similar and both belong to the 2S mode (Williamson and Roshko, 1988), they are different in two aspects. First, on the fixed cylinder the separation point remains almost unchanged during a vortex shedding cycle, whereas on the vibrating cylinder it moves back and forth due to the cylinder's motion. Second, the cross-flow distance between two successive vortices behind the vibrating cylinder is larger, whereas their streamwise distance is smaller than that behind the fixed cylinder. The reason for the latter change is because, although the oscillation of the cylinder is caused by the asymmetric vortex shedding, it in return induces more violent interactions between the upper and lower shear layers and hence expedites the shedding of asymmetric vortices.

Vortex evolution in these two cases is also quantified and shown in Fig. 6, where only the quantities associated with "positive" vortices are plotted. Behind the fixed cylinder, the normalized circulation Γ^* increases until it reaches its maximum value 4.3 at $x^* = 1.2$, indicating that the vortex is saturated around this position as shown in Fig. 6(a). After that Γ^* starts dropping quickly to 2.5 due to the vortex shedding. As the vortex convects further downstream, Γ^* continues decreasing but with a much smaller rate. As shown in Fig. 6(b), the vortex centroid first moves towards and then away from the channel centerline ($y^* = 0$). Immediately after the vortex is shed at $x^* = 1.4$, it is closest to the centerline.

Unlike in the fixed cylinder case where Γ^* monotonically increases before the vortex sheds, Γ^* behind the vibrating cylinder first increases to its maximum value 5.0 at $x^* = 0.8$, and then decreases until the vortex sheds at $x^* = 1.1$, as shown in Fig. 6(a). The reason for this increase-decrease trend is because of the change of moving direction of the cylinder. The maximum circulation is about 17% larger than that behind the fixed cylinder, which is attributed to the larger relative velocity due to the vibrating cylinder's cross-flow motion. After the vortex sheds and convects downstream, Γ^* continues decreasing. Fig. 6(b) shows that the trajectory of this vortex crosses the channel centerline. After the vortex shedding, it is farther away from the centerline compared to the trajectory behind the fixed cylinder. This magnified off-axis behavior is caused by the cross-flow flow induced by the cylinder motion.

The lift experienced by the two cylinders is time-dependent and varies with the periodical vortex shedding process. Its oscillation magnitudes ($|C_L|$) and root-mean-square values ($C_{L(rms)}$), as well as the Strouhal number (St) are listed in Table 3. The normalized vibrating amplitude of the vibrating cylinder A^* is also listed. The results reveal that the lift experienced by the vibrating cylinder is almost one order-of-magnitude larger than that experienced by the fixed cylinder, whereas the Strouhal numbers are relatively close. Allowing the cylinder to move results in an increase of the Strouhal number, meaning a faster vortex shedding rate.

Note that for the fixed cylinder slightly larger values in $|C_L|$ and St appear in the present results if compared with those listed in Table 2. These discrepancies stem from the narrower channel width used in the present simulation.

4.2. Parametric study on SJ controlled fixed cylinder

The root-mean-square (RMS) values of lift coefficient for all the 75 cases are presented in Fig. 7, which are grouped by the SJ location γ. In the following subsections, the effects of C_μ, f^* and γ will be discussed based on this figure and other additional contours/plots.

4.2.1. Effects of momentum coefficient C_μ

Fig. 7 reveals that the $C_{L(rms)}$ values for all SJ-controlled cases are smaller than those for the uncontrolled case, which demonstrates the capability of the SJs in attenuating the lift oscillation. It is also observed that $C_{L(rms)}$ monotonically decreases with increasing C_μ for a given jet frequency and location, indicating that the stronger the SJs, the better the control effect. Furthermore, $C_{L(rms)}$ approaches zero in some cases, such as the cases with γ = 30°/50°/70°, f^* = 5 and $C_\mu \geq 0.955$, and the cases with γ = 30°/50°/70°, f^* = 25 and C_μ = 2.149, meaning the lift oscillation is completely suppressed by SJs.

To further explore the effects of C_μ, the wake patterns for the uncontrolled baseline case and five representative cases with γ = 70° and f^* = 5 are compared. As shown in Fig. 8, as C_μ is relatively small (C_μ = 0 ~ 0.537), the wake is dominated by Kármán vortices. With the increase of C_μ the two shear layers developed from the cylinder elongate and the near-cylinder flow gradually becomes symmetric, as shown from Fig. 8(a) to 8(d). As a result, the $C_{L(rms)}$ value gradually decreases (refer to Fig. 7(d)). As C_μ increases further, the wake becomes the symmetric 2S mode as shown in Figs. 8(e) and 8(f), resulting in zero lift oscillations. Similar SJ-controlled wake pattern was also reported in the experimental investigations by Williams et al. (1992) and Ma et al. (2014). In addition, the present study indicates that to obtain the symmetric 2S mode and zero lift oscillation, C_μ needs to

reach a critical value between 0.537 and 0.955. This value is close to the value 0.88 reported in Williams et al. (1992) at slightly different flow and jet conditions.

The suppression or delay of the asymmetric vortex shedding is realized through two major mechanisms: First, the high-frequency SJs mitigate the evolution of large-scale vortex formation; Second, the in-phase operating SJs force synchronous vortex shedding, and hence enhance the initial symmetry of the wake. Operating in phase at $f^* = 5$, the two SJs eject five times in one natural vortex shedding period, hence interrupt the vortex shedding process five times. This phenomenon is well captured in Fig. 9, in which a time sequence of a selected case, i.e., $\gamma = 70°$, $C_\mu = 0.537$, $f^* = 5$, is presented in a close-up view, which corresponds to the case shown in Fig. 8(d). The development of a naturally shedding vortex is interrupted by the SJ ejection and as a result small pieces of symmetric vortices are generated. These small vortices then convect downstream, catch up with each other, and merge to form a large vortex as shown in Fig. 9(e).

Spectral analysis on the normalized y-component velocity $v^* = v/U_\infty$ obtained at a probe $P(1.5D, 0.5D)$ is also conducted to show the SJ effect. Fig. 10 shows the spectra for the uncontrolled case and SJ-controlled cases with $\gamma = 70°$ and $f^* = 5$. In the uncontrolled case ($C_\mu = 0$), a major peak appears at $f^* = 1$, representing the natural vortex shedding frequency. Two peaks that are at least one order-of-magnitude smaller are also observed at the harmonic frequencies. When the SJ is actuated, another peak appears at SJ operating frequency, i.e., $f^* = 5$. As C_μ increases, the peak at $f^* = 1$ reduces and the peak at $f^* = 5$ increases. When $C_\mu \geq 0.955$, the peak at $f^* = 1$ disappears, indicating the complete suppression of the natural vortex shedding, whereas the peak at $f^* = 5$ dominates the spectrum.

The vortex circulation history and vortex trajectory for two selected cases ($\gamma = 70°$, $C_\mu = 0.537$ and 0.955, $f^* = 5$) as well as the uncontrolled case are presented in Fig. 11. As for the case with $C_\mu = 0.537$, Fig. 11(a) reveals that its non-dimensional circulation Γ^* is consistently smaller than that in the uncontrolled case throughout the entire vortex evolution process. For example, its circulation at $x^* = 14$ is only about 51% of the value

in the uncontrolled case. The significant reduction of the vortex circulation after implementing jet control on a circular cylinder was also reported by Jardin and Bury (2012). In their study, opposite-signed vorticity is introduced into the shear layer through a wall-tangential pulsed jet, which directly cancels a portion of vorticity in the shear layer. In the present study, however, the circulation reduction mechanism seems different. The SJ involves both blowing and suction so that the vorticity generated in blowing is mitigated by the suction through drawing ambient vorticity-carrying fluid. The flow details in Fig. 9 reveal that the reason for the pronounced circulation reduction is because of the formation of multiple pieces of small vortices due to the SJ interruption and then the fast vorticity reduction because of viscous dissipation and vortex turning/stretching of these small vortices. Such a vortex evolution process also explains the discontinuities in vortex circulation and trajectory plotted in Fig. 11, which appear before the vortex completely sheds from the cylinder at $x^* = 3.5$. In addition, the trajectory shown in Fig. 11(b) also reveals that, by introducing the SJs, the vortex shedding position ($x^* = 3.5$) is pushed downstream from the original uncontrolled position $x^* = 1.4$. This is consistent with the elongated shear layer observed in Fig. 8(d).

As C_μ increases to 0.955 and even 2.149, the vortex is broken down by stronger SJs and the resulting smaller vortices disappear soon. As a result, the plots for circulation history and vortex trajectory are only up to about $x^* = 3$ in Fig. 11, the $C_{L(rms)}$ values are approximately zero as shown in Fig. 7(d), and the wake patterns converge to the symmetric 2S mode as shown in Fig. 8(e) and 8(f).

The above analysis confirms that the SJs are able to reduce or even eliminate the lift oscillation on the cylinder, and attenuate or even completely suppress the asymmetric wake. Such control effects are more pronounced when increasing C_μ for given f^* and γ. As C_μ exceeds a threshold value that is between 0.537 and 0.955, symmetric vortex shedding appears which is accompanied by zero lift oscillation. Furthermore, through this study it is found that the C_μ values effective in the control at very low Reynolds numbers are significantly larger than those used at high Reynolds numbers. Past investigations revealed that the SJ-like control of the wake of a circular cylinder using plasma jets or

acoustic actuators at the Reynolds number ranging from 15,000 to 33,000 only required C_μ of O(0.001) (Hsiao and Shyu, 1991; Thomas et al., 2008; Jukes and Choi, 2009). The SJ control of the wake and drag of a D-shape body at the body height based Reynolds number ranging from 23,000 to 70,000 requires C_μ of O(0.01) (Pastoor et al. 2008; Parkin et al. 2014).

4.2.2. Effect of SJ frequency f^*

Three different SJ operating frequencies, i.e., f^* = 5, 25, and 125, are studied in the present study. As shown in Fig. 7, for given C_μ and γ, $C_{L(rms)}$ increases as f^* increases. This implies that the capability of the SJs in reducing lift oscillation becomes weaker as f^* increases in the present frequency range. In some cases, such as the four cases with γ = 70° and C_μ = 0.955 plotted in Fig. 7(d), $C_{L(rms)}$ increases from zero to non-zero values as f^* increases, indicating the recurrence of asymmetric vortex shedding. To confirm this, the wake structures for the three SJ controlled cases are presented in Fig. 12 (For the sake of brevity, Fig. 12 does not include the uncontrolled case, which however can be found in Fig. 8(a)). As f^* increases from 5 to 25, the wake pattern changes from the symmetric 2S mode to the asymmetric 2S mode with an elongated shear layer as shown in Figs. 12(a) and 12(b), and as a result $C_{L(rms)}$ increases from 0 to 0.039. As f^* further increases to 125, as shown in Fig. 12(c) the wake pattern remains the asymmetric 2S mode but with a shorter shear layer (still longer than that in the uncontrolled case), and $C_{L(rms)}$ increases further to 0.102.

The effect of SJ operational frequency in the cases with a larger momentum coefficient, i.e., γ = 70° and C_μ = 2.149, is similar to that in the cases with C_μ = 0.955 as discussed above. But due to the stronger SJs the recovery of asymmetric vortex shedding with increasing f^* is less obvious. As f^* increases from 5 to 25, the wake remains symmetric as shown in Figs. 13(a) and 13(b), and $C_{L(rms)}$ remains zero. However, unlike at f^* = 5, no obvious vortex is captured in the wake at f^* = 25. As f^* increases to 125, as shown in Fig. 13(c) the wake pattern remains symmetric near the cylinder but then evolves into a weaker asymmetric 2S mode at about x^* = 6, and as a result $C_{L(rms)}$ increases from 0 to

0.018.

Fig. 14 compares the vortex circulation histories and vortex trajectories of the cases with $\gamma = 70°$ and $C_\mu = 0.955$. As f^* increases, Γ^* increases from very small values at $f^* = 5$ to values at $f^* = 125$ that are close to the uncontrolled values. In addition, the vortex trajectory at $f^* = 125$ is closest to that of the uncontrolled case as shown in Fig. 14(b). These plots again confirm that the SJ control effects become weaker as f^* increases.

Through this frequency-dependent investigation, two SJ operational modes (Ingard, 1953) are observed: the SJ mode dominated by momentum injection, and the acoustic mode dominated by propagation of sound waves. Fig. 15 shows instantaneous pseudo-Schlieren images for the cases of $f^* = 5$, 25, and 125 with $\gamma = 70°$ and $C_\mu = 0.955$. Thanks to the intrinsic compressible characteristics of the LBM, the pseudo-Schlieren images can be obtained by calculating the magnitude of density gradient (Dandois et al., 2007).

In Fig. 15(c), when the pair of SJs operates at a relatively high frequency, i.e., $f^* = 125$, very clear sound waves are observed, which propagate in all directions. The frequency of these sound waves coincides with the SJ operation frequency. In this case, the pair of SJs operates in the acoustic mode, and the energy introduced by the SJs is emitted in all directions, leaving only a small portion interacting with the shedding vortices. Hence the asymmetric shedding vortices are not affected too much by the SJs and appear very similarly to those in the uncontrolled case (compare Figs. 8(a) and 12(c)). But the wavy vortex circulation and trajectory curves shown for this case in Fig. 14 indicate that the sound wave propagation does result in small-amplitude velocity fluctuations. As the SJ operation frequency becomes as low as $f^* = 5$, the sound wave propagation is not captured in Fig. 15(a). Instead, clear periodic jet flows in the streamwise direction are observed on the leeside of the cylinder, indicating the momentum injection by the pair of SJs. In this case, the energy introduced by the SJs is mainly carried by the jet flows, and the interaction between the jet flows and the shedding vortices is strong, eliminating the natural shedding of asymmetric vortices (see Fig. 12(a)). As the SJs operate at an intermediate frequency, i.e., $f^* = 25$, both the jet flow and the sound wave propagation are

observed, suggesting that the SJs operate in a transitional mode. As a result, the wake pattern for this case falls between those at $f^* = 5$ and at $f^* = 125$, as shown in Fig. 12(b).

4.2.3. Effect of SJ position γ

From Fig. 7 the effect of SJ position γ on $C_{L(rms)}$ can also be observed. Generally, for given f^* and C_μ, $C_{L(rms)}$ values at $\gamma = 30°$, 50°, and 70° are smaller than those at $\gamma = 10°$ and 80°, indicating that the SJs located at $\gamma = 10°$ and 80° exert less control on the shedding vortices. In addition, it is interesting to see that the $C_{L(rms)}$ values at $\gamma = 10°$ are smaller than those at $\gamma = 80°$ when $f^* = 5$ and 25, whereas the trend is reversed when $f^* = 125$.

To further demonstrate the effect of SJ position γ on the wake, the flow details at a selected instant for a series of representative cases with $C_\mu = 0.537$ and $f^* = 5$ are shown in Fig. 16. From the close view images in the left column, it is confirmed that each SJ produces a vortex pair during one operation period, and it is this pair of vortices that interacts with the shear layers and performs flow control. In the case with $\gamma = 10°$ as shown in Fig. 16(b1), the two SJ actuators are very close to the cylinder's horizontal centerline and away from the two shear layers. In addition, the two produced SJs are so close to each other that the two inner branches of their vortex pairs cancel out with each other. As a result, the SJ strength is reduced. For these reasons, it is not surprising to see that the SJ control effect in this case is significantly less compared to those in the cases with $\gamma = 30°$, 50°, and 70°, as demonstrated in the wake patterns shown in the right column of Fig. 16.

On the other hand, in the case with $\gamma = 80°$ the two SJ actuators are located far upstream of the mean separation points (at about $\gamma = 58°$) of the shear layers, and hence the produced SJs are deeply immersed in the shear layers all the time. The strong vorticity carried by the shear layers effectively suppresses the production of the upstream branch of the SJs. Therefore, much smaller and weaker vortices are produced by the SJs in this case as shown in Fig. 16(f1), and their control effect is also significantly discounted as

shown in Fig. 16(f2).

In the rest of cases with γ = 30°, 50° and 70°, the SJ actuators are located either slightly downstream or slightly upstream of the mean separation points of the shear layers. The wake patterns shown in Fig. 16 and the $C_{L(rms)}$ values plotted in Fig. 7 reveal that at these locations the SJs can sufficiently interact with the shear layers and are able to effectively control the asymmetric vortex shedding.

The evolution of vortex circulation and trajectory for cases with three representative SJ positions, i.e., γ = 10°, 30°, and 70°, is plotted in Fig. 17. It is found that the evolution in the γ = 10° case is very similar to that in the uncontrolled case, whereas the evolution in the γ = 30° case is similar to those in the γ = 70° case. This is consistent with the wake pattern observation from Fig. 16. Note that there are obvious differences between the γ = 30° and γ = 70° cases in the vortex evolution before about x^* = 8. The break-up of the shedding vortex happens earlier and more discontinuities appear in the γ = 70° case. This is because the SJ actuators at γ = 70° are closer to the mean separation points of the shear layers, and hence they are able to exert more influence on the shear layers.

4.3. SJ-controlled vortex-induced oscillating cylinder

As described in Section 2.2, by allowing the cylinder to move in the cross-flow direction with the support of a spring-damper system, the cylinder oscillates under the excitation of asymmetrically shedding vortices. To control this one-dimensional VIV, a pair of SJs is applied which operates at the same set of operating conditions (C_μ, f^*, and γ) as for the fixed cylinder in Section 4.2. Among the 75 cases, it is found that the cross-flow oscillation of the cylinder can be completely suppressed only in three cases, i.e., with C_μ = 2.149, f^* = 5, and γ = 30°, with C_μ = 2.149, f^* = 5, and γ = 50°, and with C_μ = 2.149, f^* = 25, and γ = 50°. This indicates that, to completely suppress the one-dimensional VIV, the SJ momentum coefficient must be no less than C_μ = 2.149, the position of the SJ actuators should be at γ = 30° or 50°, and the SJ operating frequency is either f^* = 5 or 25. This SJ operational range is much narrower compared to that for the fixed cylinder cases in which

the lift oscillation can be completely suppressed, i.e., $C_{L(rms)} = 0$. There are two reasons for this reduction of the effective operational range. First, the transverse motion of the cylinder induces greater relative flow speed around the cylinder, resulting in shear layers with larger vorticity. The stronger shear layers then require stronger SJs for the control. Second, the motion of the cylinder causes the mean separation points of shear layers to move further downstream on the cylinder. As such, in most of the time the SJ actuators at $\gamma = 70°$ are immersed in the shear layers. As a result, none of the cases with $\gamma = 70°$ can completely suppress the VIV of the cylinder.

To demonstrate the SJ control effectiveness, the case with $C_\mu = 2.149$, $f^* = 5$, and $\gamma = 30°$ is presented here. The time history of the cross-flow location of the cylinder center is plotted in Fig. 18(a), where points (a) to (i) indicate the instants corresponding to the snapshots of wake structures shown in Figs. 19(a) to 19(i), respectively. The SJs are actuated when the cylinder is passing through point (d) at $t^* = t/T = 0$ and $y^* = y/A = 0$, at which the spring is at its original length. After that, the cylinder keeps moving upward and reaches the highest point (e) at $t^* = 0.267$. At this instant, $y^* = 0.542$, slightly less than the value 0.545 at point (a), but the shear layer detached from the upper surface of the cylinder (in blue) has been broken into two pieces by the SJs, if comparing the wake patterns shown in Figs. 19(a) and 19(e). At $t^* = 0.618$ when the cylinder moves back to the its equilibrium position, point (f), that shear layer is totally separated from its downstream portion, while the shear layer detached from the lower surface (in red) has been broken into several pieces by the SJ pair, if comparing the wake patterns shown in Figs. 19(b) and 19(f). As the cylinder continues moving downward, it reaches the lowest point (g) $y^* = -0.168$ at $t^* = 0.816$, which is only 31% of the uncontrolled value ($y^* = -0.545$) at point (c). Besides, the shear layers detached from the cylinder are completely disrupted by the SJs, if comparing the vorticity contours shown in Figs. 19(c) and 19(g). At $t^* = 1.070$, the cylinder moves back to its equilibrium position again, represented by point (h). At this instant, the uncontrolled shear layers shown in Fig. 19(d) are replaced by a series of SJ produced vortices as shown in Fig. 19(h). As this SJ control continues, the oscillation amplitude of the cylinder keeps decreasing, and finally approaches zero at $t^* = 4.000$, meaning the one-dimensional VIV of the cylinder has been completely

suppressed. At this instant, the wake pattern behind the cylinder becomes the symmetric 2S mode as shown in Fig. 19(i).

The effect of the SJ actuation timing is also studied. Three additional cases operating with C_μ = 2.149, f^* = 5, and γ = 30° are investigated, in which the SJs are actuated when the cylinder is at the position corresponding to points (1), (3) and (4) as indicated in Fig. 18(b). The time histories of the cylinder's cross-flow position plotted in Fig. 18(b) reveal that in all the four cases the SJs are able to successively suppress the oscillation of the cylinder within three natural vortex shedding periods, suggesting that the one-dimensional VIV control using the present SJ configurations is not sensitive to the SJ actuation timing. This finding is useful for future investigations on SJ flow control using feedback control schemes.

5. Conclusion

In this paper, active control of the wakes and one-dimensional VIVs of a single circular cylinder using a pair of SJs is conducted at a low Reynolds number of Re = 100. An LBM based numerical framework is established to facilitate this study, in which the multi-block scheme and the overlap-mesh approach with improved information exchange mechanisms are used to balance the computational accuracy and efficiency, and the interpolated bounce-back scheme and a corrected momentum exchange scheme are adopted for accurate force evaluation.

Two cylinder configurations are investigated. In the first configuration, the cylinder is fixed, on which a pair of in-phase operating SJs is implemented. The effects of three key parameters of the SJ pair, i.e., momentum coefficient C_μ, frequency f^*, and position γ, on the wake pattern behind the cylinder and the lift oscillation experienced by the cylinder are investigated. Main findings from this parametric study are as follows:

(i) The control effect increases with the increase of C_μ. That is, the Kármán vortex street behind the cylinder is gradually replaced by symmetric 2S vortices or even no vortex shedding. As a result, the lift oscillation gradually reduces to zero.

(ii) To achieve effective SJ control, the required C_μ at the present low Reynolds number (Re = 100) is found be much larger than that required at high Reynolds numbers (Re = O(10^5)).

(iii) Among the three frequencies considered in the present study, it is found that the SJs operating at $f^* = 5$ give the best control effect. The reason is that at this frequency the SJs operate in the momentum-injection mode, in which most of the energy is injected into the wake, whereas at the highest frequency, i.e., $f^* = 125$, the SJs operate in the acoustic mode, in which most of the energy is emitted in all directions through sound waves.

(iv) It is found that the SJ pair works effectively at around the quarter arc edge of the cylinder's leeward side, i.e., $\gamma = 30°$, 50° and 70°. If the SJ actuators are located close to the cylinder's horizontal centerline, i.e., $\gamma = 10°$, the SJs are far away from the shear layers and hence have little control effect. If the SJ actuators are located near the cylinder's vertical centerline, i.e., $\gamma = 80°$, the SJs are deep immersed in the shear layers and the injected vorticity flux are impaired by the strong surrounding shear, hence their control effect is significantly discounted.

In the second configuration, the same cylinder oscillates in the cross-flow direction under the excitation of asymmetrically shedding vortices and the constraint of a spring. The same set of parameter combinations as in the first configuration is applied on this cylinder. It is found that not all the parameter combinations that completely suppress the lift oscillation on the fixed cylinder are able to completely suppress the one-dimensional VIV of the oscillating cylinder. The reason stems from the increased relative motion between the cylinder and its surrounding flow due to the cylinder's cross-flow motion, leading to the shedding of stronger vortices. The suppression of one-dimensional VIV is well demonstrated by the use of the SJ control with three parameter combinations. It is also found that the VIV control using the present SJs is not sensitive to the SJ actuation timing. Furthermore, through the present study more flow details about SJ-controlled flow around the cylinder and in the wakes are revealed.

In the near future, two logical extensions of the present work will be conducted: 1. To

investigate new lock-on phenomena at lower frequencies around $f^* \approx 1; 2$. To suppress two-dimensional VIVs of a circular cylinder using SJs plus other control means.

Reference

Ahn, H.T., Kallinderis, Y., 2006. Strongly coupled flow/structure interactions with a geometrically conservative ALE scheme on general hybrid meshes. Journal of Computational Physics 219, 671-696.

Anderson, C.S., Semercigil, S.E., Turan, Ö.F., 2005. Vibration suppression of stepped beams: new designs for hot-wire probes. Journal of Sound and Vibration 282, 197-214.

Atta, C.W.V., Gharib, M., 1987. Ordered and chaotic vortex streets behind circular cylinders at low Reynolds numbers. Journal of Fluid Mechanics 174, 113-133.

Borazjani, I., Ge, L., Sotiropoulos, F., 2008. Curvilinear immersed boundary method for simulating fluid structure interaction with complex 3D rigid bodies. Journal of Computational physics 227, 7587-7620.

Chen, S., Doolen, G.D., 1998. Lattice Boltzmann method for fluid flows. Annual review of fluid mechanics 30, 329-364.

Chen, Y., Cai, Q., Xia, Z., Wang, M., Chen, S., 2013. Momentum-exchange method in lattice Boltzmann simulations of particle-fluid interactions. Physical Review E 88, 013303.

Choi, H., Jeon, W.-P., Kim, J., 2008. Control of flow over a bluff body. Annu. Rev. Fluid Mech. 40, 113-139.

Choi, J.-I., Oberoi, R.C., Edwards, J.R., Rosati, J.A., 2007. An immersed boundary method for complex incompressible flows. Journal of Computational Physics 224, 757-784.

Dandois, J., Garnier, E., Sagaut, P., 2007. Numerical simulation of active separation control by a synthetic jet. Journal of Fluid Mechanics 574, 25-58.

Feng, L., Wang, J., 2010. Circular cylinder vortex-synchronization control with a synthetic jet positioned at the rear stagnation point. Journal of Fluid Mechanics 662, 232-259.

Feng, L., Wang, J., 2012. Synthetic jet control of separation in the flow over a circular cylinder. Experiments in fluids 53, 467-480.

Feng, L., Wang, J., 2014a. Modification of a circular cylinder wake with synthetic jet: Vortex shedding modes and mechanism. European Journal of Mechanics - B/Fluids 43, 14-32.

Feng, L., Wang, J., 2014b. The virtual aeroshaping enhancement by synthetic jets with variable suction and blowing cycles. Physics of Fluids (1994-present) 26, 014105.

Feng, L., Wang, J., Pan, C., 2010. Effect of novel synthetic jet on wake vortex shedding modes of a circular cylinder. Journal of Fluids and Structures 26, 900-917.

Ginzburg, I., d'Humières, D., 2003. Multireflection boundary conditions for lattice Boltzmann models. Physical Review E 68, 066614.

Hsiao, F.B., Shyu, J.Y., 1991. Influence of internal acoustic excitation upon flow passing a circular cylinder. Journal of Fluids and Structures 5, 427-442.

Ingard, U., 1953. On the Theory and Design of Acoustic Resonators. The Journal of the Acoustical Society of America 25, 1037-1061.

Izquierdo, S., Fueyo, N., 2008. Characteristic nonreflecting boundary conditions for open boundaries in lattice Boltzmann methods. Physical Review E 78, 046707.

Jardin, T., Bury, Y., 2012. Lagrangian and spectral analysis of the forced flow past a circular cylinder using pulsed tangential jets. Journal of Fluid Mechanics 696, 285-300.

Jiang, R., Lin, J., Chen, Z., 2013. Vibrations of cylindrical objects obstructing a Poiseuille-type flow. Physical Review E 88, 023009.

Jukes, T.N., Choi, K.-S., 2009. Flow control around a circular cylinder using pulsed dielectric barrier discharge surface plasma. Physics of Fluids (1994-present) 21, 084103.

Lallemand, P., Luo, L.-S., 2000. Theory of the lattice Boltzmann method: Dispersion, dissipation, isotropy, Galilean invariance, and stability. Physical Review E 61, 6546-6562.

Lallemand, P., Luo, L.-S., 2003. Lattice Boltzmann method for moving boundaries. Journal of Computational Physics 184, 406-421.

Liu, C., Zheng, X., Sung, C.H., 1998. Preconditioned multigrid methods for unsteady incompressible flows. Journal of Computational Physics 139, 35-57.

Ma, L., Feng, L., Liu, L., Wang, J., 2014. Experimental investigation on the flow around a circular cylinder controlled by synthetic jets, Paper No. 1051, 16th International Symposium on Flow Visualization, Okinawa, Japan.

Meldi, M., Vergnault, E., Sagaut, P., 2013. An arbitrary Lagrangian-Eulerian approach for the simulation of immersed moving solids with Lattice Boltzmann Method. Journal of Computational Physics 235, 182-198.

Munday, P.M., Taira, K., 2013. On the lock-on of vortex shedding to oscillatory actuation around a circular cylinder. Physics of Fluids (1994-present) 25, 013601.

Pavlova, A.A., Otani, K., Amitay, M., 2008. Active control of sprays using a single synthetic jet actuator, International Journal of Heat and Fluid Flow 29, 131–148.

Parkin, D.J., Thompson, M.C., Sheridan, J., 2014. Numerical analysis of bluff body wakes under periodic open-loop control, Jounral of Fluid Mechanics 739, 94-123.

Pastoor, M., Henning, L., Noack, B.R., King, R., Tadmor, G., 2008. Feedback shear layer control for bluff body drag reduction, Journal of Fluid Mechanics 608, 161-196.

Perry, A.E., Morrison, G.L., 1971. Vibration of hot-wire anemometer filaments. Journal of Fluid Mechanics 50, 815-825.

Tang, H., Salunkhe, P., Zheng, Y., Du, J., Wu, Y., 2014. On the use of synthetic jet actuator arrays for active flow separation control, Experimental Thermal and Fluid Science 57, 1-10.

Thomas, F.O., Kozlov, A., Corke, T.C., 2008. Plasma Actuators for Cylinder Flow Control and Noise Reduction. AIAA Journal 46, 1921-1931.

Wang, J.J., Feng, L.H., Xu, C.J., 2007. Experimental investigations on separation control and flow structure around a circular cylinder with synthetic jet, Science in China, Series E: Technological Sciences 50, 550–559.

Williams, D.R., Mansy, H., Amato, C., 1992. The response and symmetry properties of a cylinder wake subjected to localized surface excitation. Journal of Fluid Mechanics 234, 71-96.

Williamson, C., 1989. Oblique and parallel modes of vortex shedding in the wake of a circular cylinder at low Reynolds numbers. Journal of Fluid Mechanics 206, 579-627.

Williamson, C., 1996. Three-dimensional wake transition. Journal of Fluid Mechanics 328, 345-407.

Williamson, C., Roshko, A., 1988. Vortex formation in the wake of an oscillating cylinder. Journal of fluids and structures 2, 355-381.

Yu, D., 2002. Viscous flow computations with the lattice-Boltzmann equation method. University of Florida.

Zhou, J., Adrian, R., Balachandar, S., Kendall, T., 1999. Mechanisms for generating coherent packets of hairpin vortices in channel flow. Journal of Fluid Mechanics 387, 353-396.

Table captions

Table 1. Selected SJ values for the parametric study.

Table 2. Comparison of the oscillation magnitude of lift coefficient and Strouhal number at Re = 100.

Table 3. Oscillation magnitudes and root-mean-square values of lift coefficient, Strouhal numbers, and the normalized oscillation amplitude of the uncontrolled cylinder.

Tables

Table 1. Selected SJ values for the parametric study.

C_μ	f^*	γ
0.060		10°
0.239	5	30°
0.537	25	50°
		70°
0.955	125	80°
2.149		

Table 2. Comparison of the oscillation magnitude of lift coefficient and Strouhal number at $Re = 100$.

Reference	Methodology	$\lvert C_L \rvert$	St
Williamson (1989)	Experiment	--	0.166
Liu et al. (1998)	NS	0.339	0.164
Choi et al. (2007)	NS	0.315	0.164
Present	LBM	0.329	0.166

Table 3. Oscillation magnitudes and root-mean-square values of lift coefficient, Strouhal numbers, and the normalized oscillation amplitude of the uncontrolled cylinder.

Cases	$\lvert C_L \rvert$	$C_{L(rms)}$	St	A^*
Fixed cylinder	0.337	0.238	0.169	--
Vibrating cylinder	2.962	2.109	0.186	0.545

Figure captions

Fig. 1. Schematic of a fixed cylinder equipped with a SJ pair. The two short red line sections represent the SJ pair; U_∞ is the freestream velocity; D is the cylinder diameter; d is the SJ width; β describes the orientation of the SJs; γ describes the location of the SJs; $\boldsymbol{u}_{sj}^{u}$ and $\boldsymbol{u}_{sj}^{l}$ are the velocities of the upper and lower SJs, respectively; Point P located at (1.5D, 0.5D) is a detection point.

Fig. 2. Schematic of the passively oscillating cylinder equipped with a SJ pair. The two red line sections represent the SJ pair; U_∞ is the freestream velocity; D is the diameter of the cylinder; ρ_c is the density of the cylinder; $\boldsymbol{u}_{w}^{cm}$ is the translational velocity of the cylinder; $\boldsymbol{u}_{sj}^{u}$ and $\boldsymbol{u}_{sj}^{l}$ are the velocities of the upper and lower SJs relative to the oscillating cylinder, respectively; K is the stiffness of the spring; and C is the damping factor.

Fig. 3. Computational domain with multi-block arrangement (not in scale).

Fig. 4. Normalized maximum amplitude $A^* = A_{max}/D$ of the cylinder against reduced velocity U_R.

Fig. 5. Wake patterns of (a) unforced fixed-cylinder case and (b) unforced oscillating-cylinder case. The contour is normalized vorticity ω^*. The solid and dash lines represent vortices identified by λ_{ci} = 0.2 isolines enclosing positive and negative vorticity, respectively.

Fig. 6. Evolution of (a) normalized vortex circulation Γ^* and (b) normalized vortex position $y^* = y/D$ against streamwise position $x^* = x/D$. Symbols ■ and □ represent the unforced fixed and oscillating cylinder cases, respectively.

Fig. 7 Variation of root-mean-square values of lift coefficient, $C_{L(rms)}$, against the momentum coefficient, C_μ, for the SJ pair placed at γ = (a) 10°; (b) 30°; (c) 50°; (d) 70°; (e) 80°.

Fig. 8. Wake patterns of (a) unforced case; (b) γ = 70°, C_μ = 0.060, f^* = 5; (c) γ = 70°, C_μ = 0.239, f^* = 5; (d) γ = 70°, C_μ = 0.537, f^* = 5; (e) γ = 70°, C_μ = 0.955, f^* = 5; (f) γ = 70°, C_μ = 2.149, f^* = 5. The contour is normalized vorticity ω^*. The solid and dash lines represent vortices identified by λ_{ci} = 0.2 isolines enclosing positive and negative vorticity, respectively. Refer to Fig. 5(a) for the colorbar.

Fig. 9. Evolution of wake pattern within one natural vortex shedding period for the case of γ = 70°, C_μ = 0.537 and f^* = 5 at five different instants: (a) t = 0.2T; (b) t = 0.4T; (c) t = 0.6T; (d) t = 0.8T; (e) t = 1.0T. The contour is normalized vorticity ω^*. The solid and dash lines represent vortices identified by λ_{ci} = 0.2 isolines enclosing positive and negative vorticity, respectively. Refer to Fig. 5(a) for the colorbar. “A”

denotes anti-clockwise vortices, the superscript "-1" denotes the identified vortices shed in the previous period, and the subscripts denotes the original piece number of vortices shed in the current period. For instance, A_{1+2+3} represents a new vortex that forms through the combination of vortices A_1, A_2 and A_3 shed in the current period.

Fig. 10. Spectral analysis of normalized y-component velocity $v^* = v/U_\infty$ probed at $P(1.5D,0.5D)$. $\gamma = 70°$, $f^* = 5$.

Fig. 11. Evolution of (a) normalized vortex circulation Γ^* and (b) normalized vortex position $y^* = y/D$ against streamwise position $x^* = x/D$. Symbols ■, ◇ and + represent the unforced case, case with $\gamma = 70°$, $C_\mu = 0.537$, $f^* = 5$, and case with $\gamma = 70°$, $C_\mu = 0.955$, $f^* = 5$, respectively.

Fig. 12. Wake patterns for (a) $C_\mu = 0.955$, $f^* = 5$, $\gamma = 70°$; (b) $C_\mu = 0.955$, $f^* = 25$, $\gamma = 70°$; (c) $C_\mu = 0.955$, $f^* = 125$, $\gamma = 70°$. The contour is normalized vorticity ω^*. The solid and dash lines represent vortices identified by $\lambda_{ci} = 0.2$ isolines enclosing positive and negative vorticity, respectively. Refer to Fig. 5(a) for the colorbar.

Fig. 13. Wake patterns for (a) $\gamma = 70°$, $C_\mu = 2.149$, $f^* = 5$; (b) $\gamma = 70°$, $C_\mu = 2.149$, $f^* = 25$; (c) $\gamma = 70°$, $C_\mu = 2.149$, $f^* = 125$. The contour is normalized vorticity ω^*. The solid and dash lines represent vortices identified by $\lambda_{ci} = 0.2$ isolines enclosing positive and negative vorticity, respectively. Refer to Fig. 5(a) for the colorbar.

Fig. 14. Evolution of (a) normalized vortex circulation Γ^* and (b) normalized vortex position $y^* = y/D$ against streamwise position $x^* = x/D$. Symbols ■, +, ○, and Δ represent the unforced case; $\gamma = 70°$, $C_\mu = 0.955$, $f^* = 5$; $\gamma = 70°$, $C_\mu = 0.955$, $f^* = 25$; $\gamma = 70°$, $C_\mu = 0.955$, $f^* = 125$, respectively.

Fig. 15. Instantaneous pseudo-Schlieren visualization: $\gamma = 70°$, $C_\mu = 0.955$, and (a) $f^* = 5$; (b) $f^* = 25$; (c) $f^* = 125$. For better presentation, the contour scale in (c) is 10 times of those in (a) and (b).

Fig. 16. Near and far field wake patterns: (a) unforced case; (b) $C_\mu = 0.537$, $f^* = 5$, $\gamma = 10°$; (c) $C_\mu = 0.537$, $f^* = 5$, $\gamma = 30°$; (d) $C_\mu = 0.537$, $f^* = 5$, $\gamma = 50°$; (e) $C_\mu = 0.537$, $f^* = 5$, $\gamma = 70°$; (f) $C_\mu = 0.537$, $f^* = 5$, $\gamma = 80°$. The contour is normalized vorticity ω^*. The solid and dash lines represent vortices identified by $\lambda_{ci} = 0.2$ isolines enclosing positive and negative vorticity, respectively. Refer to Fig. 5(a) for the colorbar.

Fig. 17. Evolution of (a) normalized vortex circulation Γ^* and (b) normalized vortex position $y^* = y/D$ against streamwise position $x^* = x/D$. Symbols ■, ∇, × and ◇ represent the unforced case; $\gamma = 10°$, $C_\mu = 0.537$, $f^* = 5$; $\gamma = 30°$, $C_\mu = 0.537$, $f^* = 5$; $\gamma = 70°$, $C_\mu = 0.537$, $f^* = 5$, respectively.

Fig. 18. Time history of the cross-flow position of the oscillating cylinder: (left) when the SJs are actuated at point (d); (right) when the SJs are actuated at points (1) to (4).

Fig. 19. Snapshots of cylinder position and wake patterns: (a) to (i) correspond to points (a) to (i) in Fig. 18 (a). The contour is normalized vorticity ω^*. The solid and dash lines represent vortices identified by λ_{ci} = 0.2 isolines enclosing positive and negative vorticity, respectively. Refer to Fig. 5(a) for the colorbar.

Figures

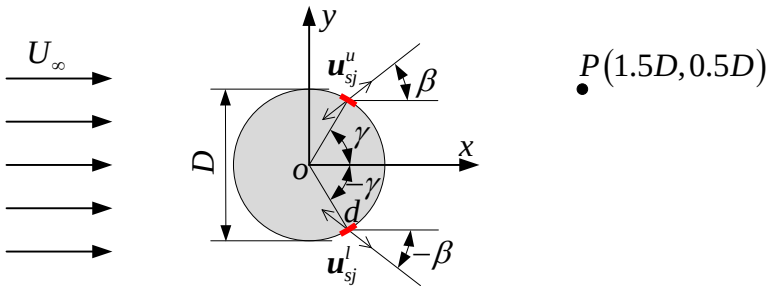

Fig. 1. Schematic of a fixed cylinder equipped with a SJ pair. The two short red line sections represent the SJ pair; U_∞ is the freestream velocity; D is the cylinder diameter; d is the SJ width; β describes the orientation of the SJs; γ describes the location of the SJs; $\boldsymbol{u}_{sj}^{u}$ and $\boldsymbol{u}_{sj}^{l}$ are the velocities of the upper and lower SJs, respectively; Point P located at (1.5D, 0.5D) is a detection point.

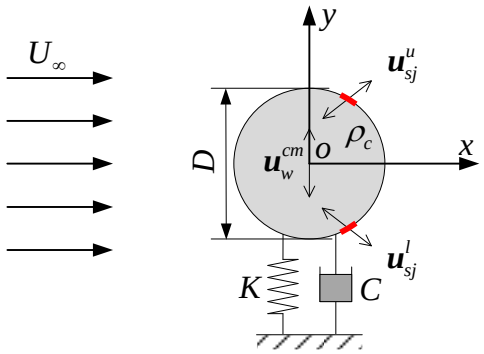

Fig. 2. Schematic of the passively oscillating cylinder equipped with a SJ pair. The two red line sections represent the SJ pair; U_∞ is the freestream velocity; D is the diameter of the cylinder; ρ_c is the density of the cylinder; $\boldsymbol{u}_w^{cm}$ is the translational velocity of the cylinder; $\boldsymbol{u}_{sj}^{u}$ and $\boldsymbol{u}_{sj}^{l}$ are the velocities of the upper and lower SJs relative to the oscillating cylinder, respectively; K is the stiffness of the spring; and C is the damping factor.

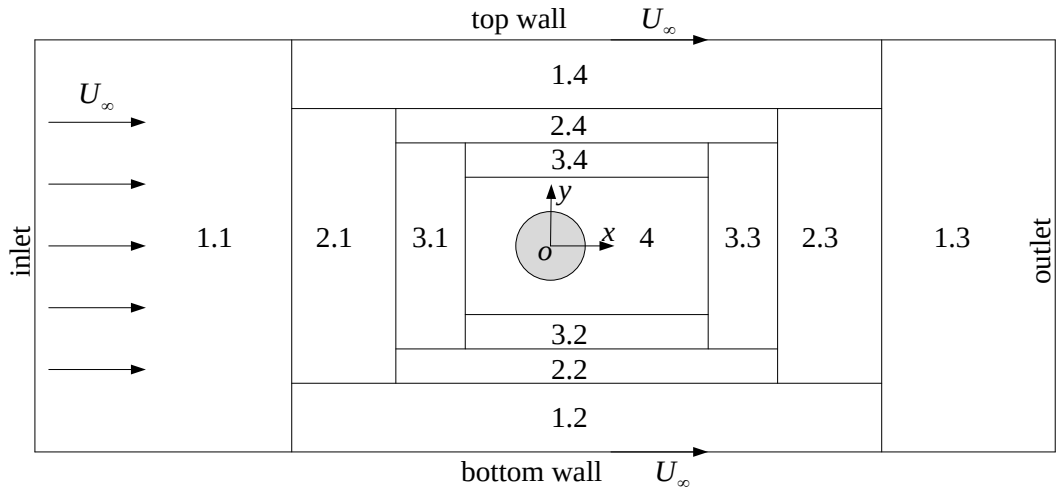

Fig. 3. Computational domain with multi-block arrangement (not in scale).

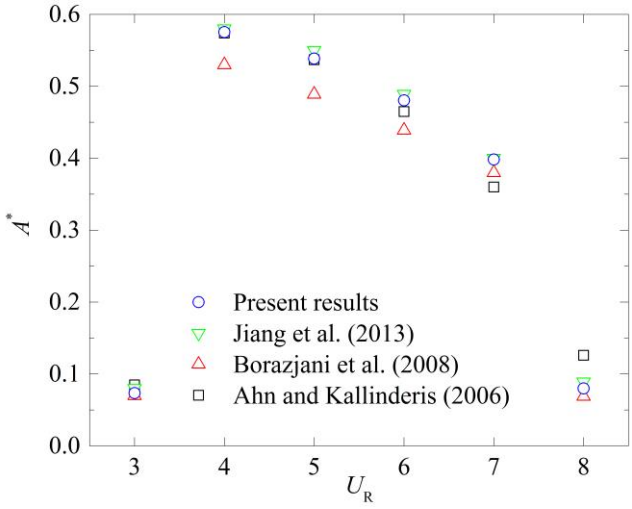

Fig. 4. Normalized maximum amplitude $A^* = A_{max}/D$ of the cylinder against reduced velocity U_R.

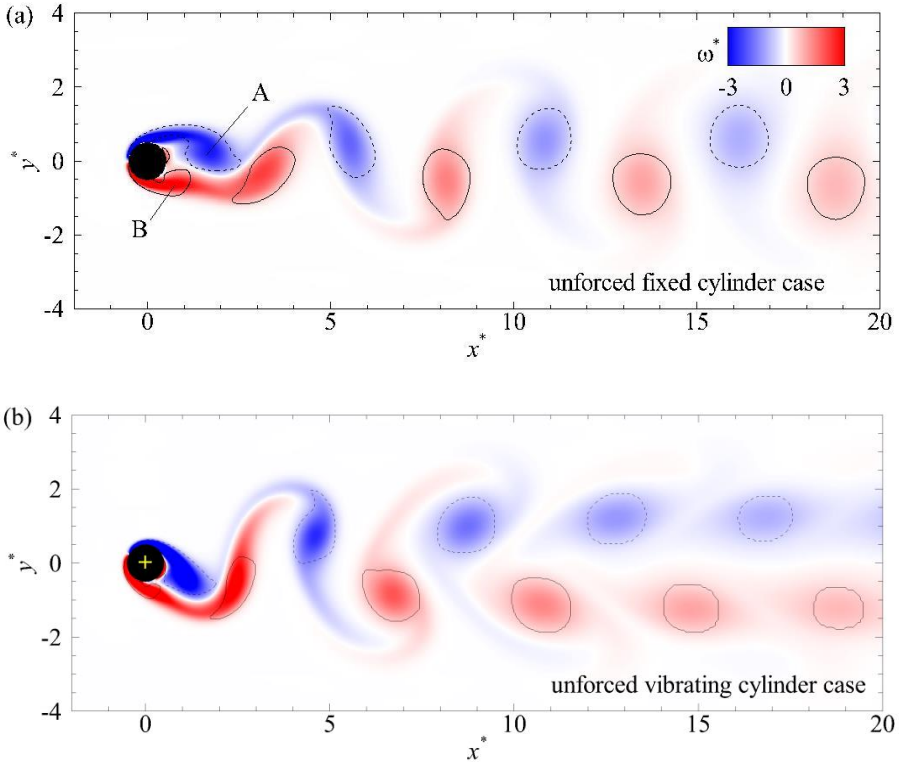

Fig. 5. Wake patterns of (a) unforced fixed-cylinder case and (b) unforced oscillating-cylinder case. The contour is normalized vorticity ω^*. The solid and dash lines represent vortices identified by λ_{ci} = 0.2 isolines enclosing positive and negative vorticity, respectively.

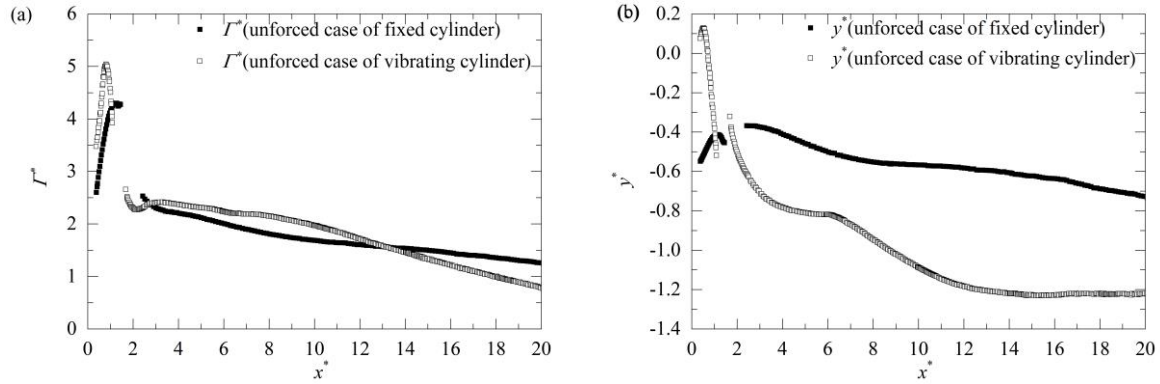

Fig. 6. Evolution of (a) normalized vortex circulation Γ^* and (b) normalized vortex position $y^* = y/D$ against streamwise position $x^* = x/D$. Symbols ■ and □ represent the unforced fixed and oscillating cylinder cases, respectively.

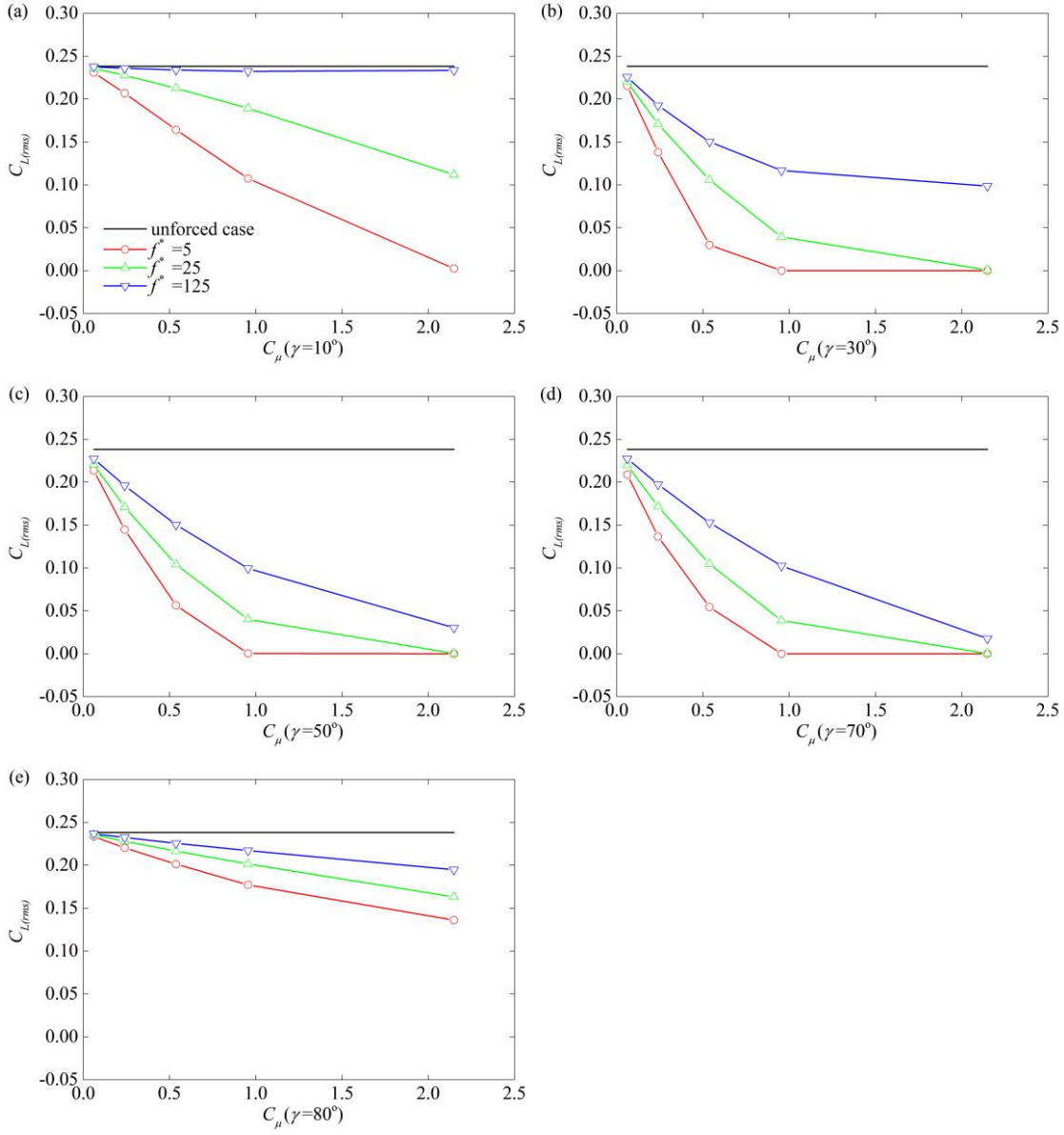

Fig. 7 Variation of root-mean-square values of lift coefficient, $C_{L(rms)}$, against the momentum coefficient, C_μ, for the SJ pair placed at γ = (a) 10°; (b) 30°; (c) 50°; (d) 70°; (e) 80°.

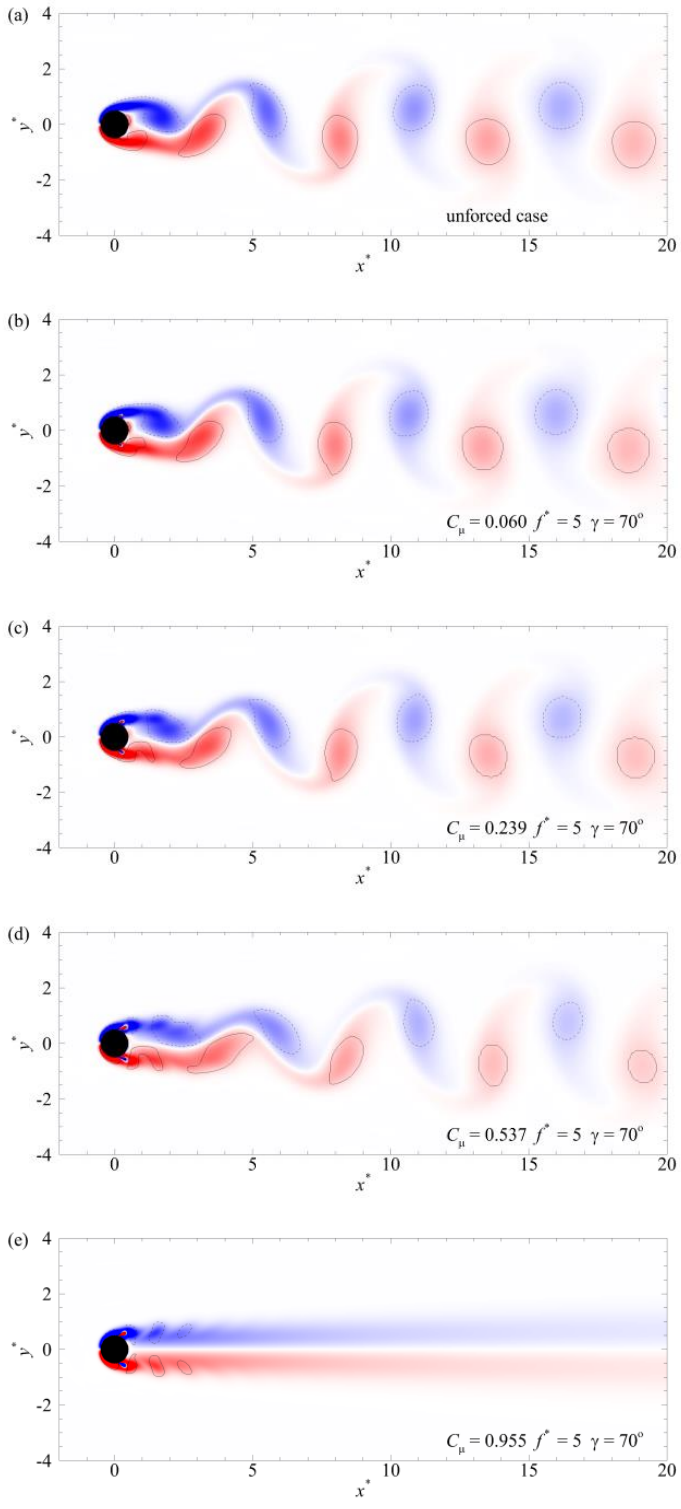
(a)
unforced case
(b)
$C_\mu = 0.060$ $f^* = 5$ $\gamma = 70^o$
(c)
$C_\mu = 0.239$ $f^* = 5$ $\gamma = 70^o$
(d)
$C_\mu = 0.537$ $f^* = 5$ $\gamma = 70^o$
(e)
$C_\mu = 0.955$ $f^* = 5$ $\gamma = 70^o$
x^*
y^*

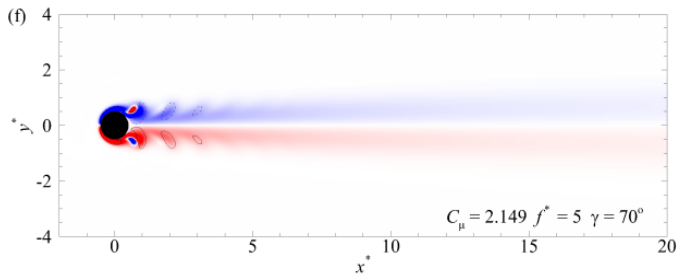

Fig. 8. Wake patterns of (a) unforced case; (b) γ = 70°, C_μ = 0.060, f^* = 5; (c) γ = 70°, C_μ = 0.239, f^* = 5; (d) γ = 70°, C_μ = 0.537, f^* = 5; (e) γ = 70°, C_μ = 0.955, f^* = 5; (f) γ = 70°, C_μ = 2.149, f^* = 5. The contour is normalized vorticity ω^*. The solid and dash lines represent vortices identified by λ_{ci} = 0.2 isolines enclosing positive and negative vorticity, respectively. Refer to Fig. 5(a) for the colorbar.

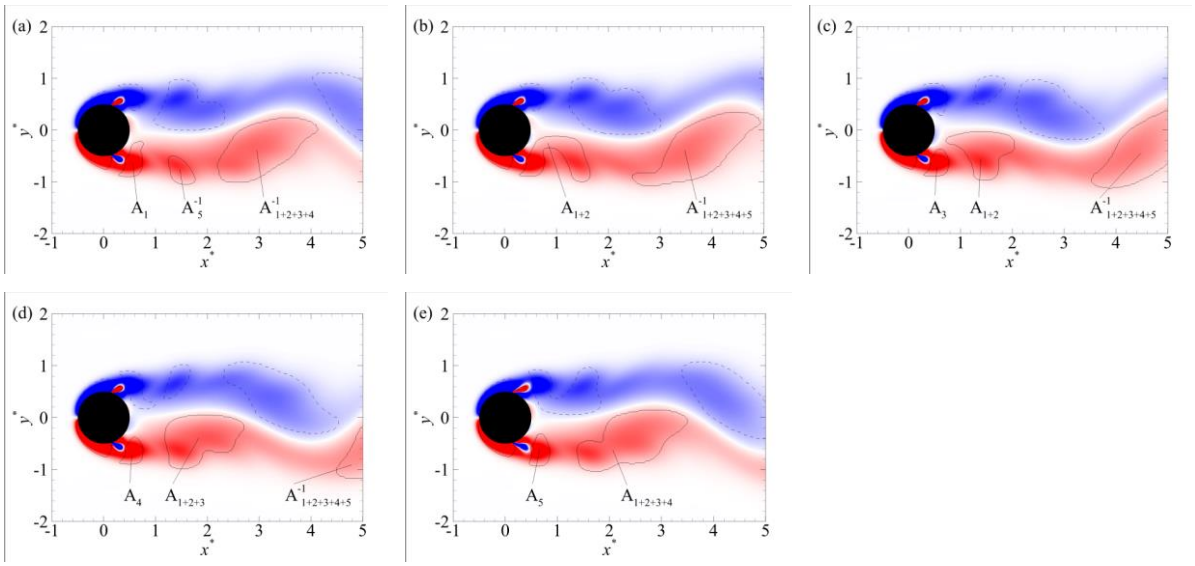

Fig. 9. Evolution of wake pattern within one natural vortex shedding period for the case of γ = 70°, C_μ = 0.537 and f^* = 5 at five different instants: (a) t = 0.2T; (b) t = 0.4T; (c) t = 0.6T; (d) t = 0.8T; (e) t = 1.0T. The contour is normalized vorticity ω^*. The solid and dash lines represent vortices identified by λ_{ci} = 0.2 isolines enclosing positive and negative vorticity, respectively. Refer to Fig. 5(a) for the colorbar. "A" denotes anti-clockwise vortices, the superscript "-1" denotes the identified vortices shed in the previous period, and the subscripts denotes the original piece number of vortices shed in the current period. For instance, A_{1+2+3} represents a new vortex that forms through the combination of vortices A_1, A_2 and A_3 shed in the current period.

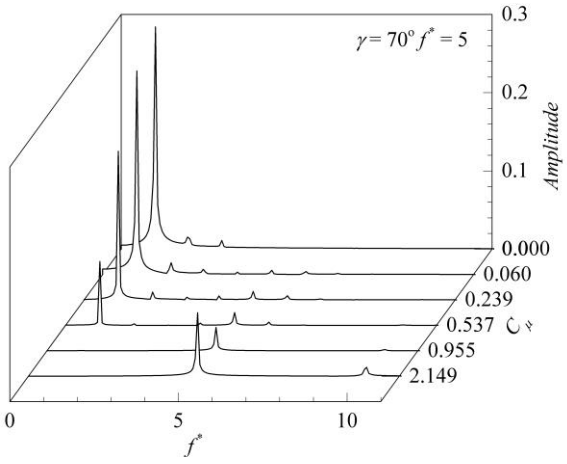

Fig. 10. Spectral analysis of normalized y-component velocity $v^* = v/U_\infty$ probed at $P(1.5D,0.5D)$. $\gamma = 70°$, $f^* = 5$.

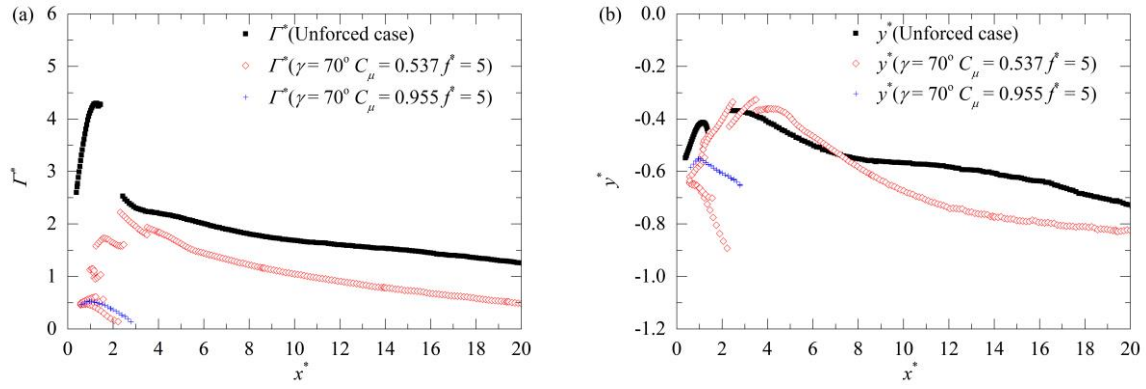

Fig. 11. Evolution of (a) normalized vortex circulation Γ^* and (b) normalized vortex position $y^* = y/D$ against streamwise position $x^* = x/D$. Symbols ■, ◇ and + represent the unforced case, case with $\gamma = 70°$, $C_\mu = 0.537$, $f^* = 5$, and case with $\gamma = 70°$, $C_\mu = 0.955$, $f^* = 5$, respectively.

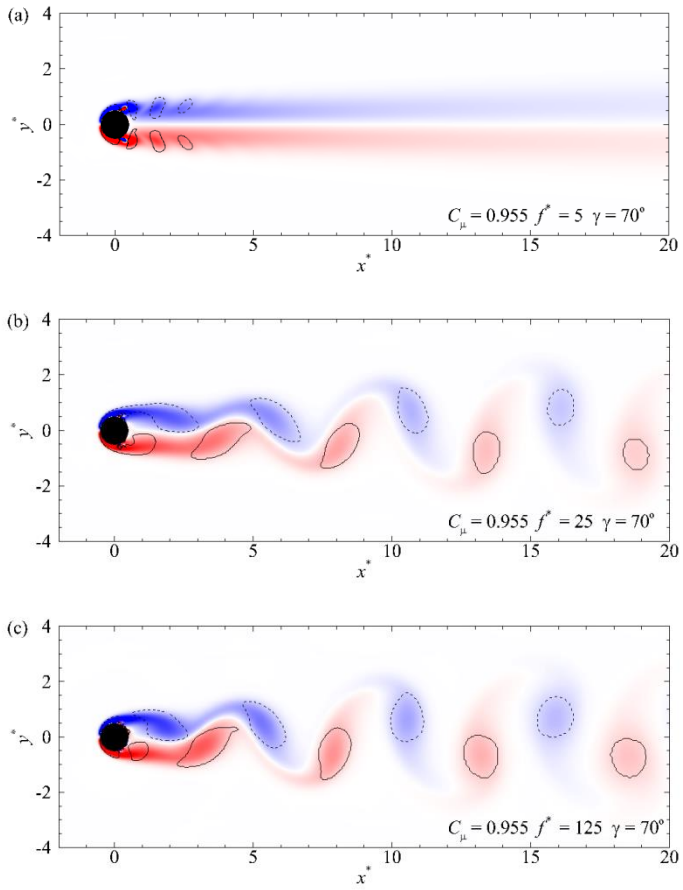

Fig. 12. Wake patterns for (a) C_μ = 0.955, f^* = 5, γ = 70°; (b) C_μ = 0.955, f^* = 25, γ = 70°; (c) C_μ = 0.955, f^* = 125, γ = 70°. The contour is normalized vorticity ω^*. The solid and dash lines represent vortices identified by λ_{ci} = 0.2 isolines enclosing positive and negative vorticity, respectively. Refer to Fig. 5(a) for the colorbar.

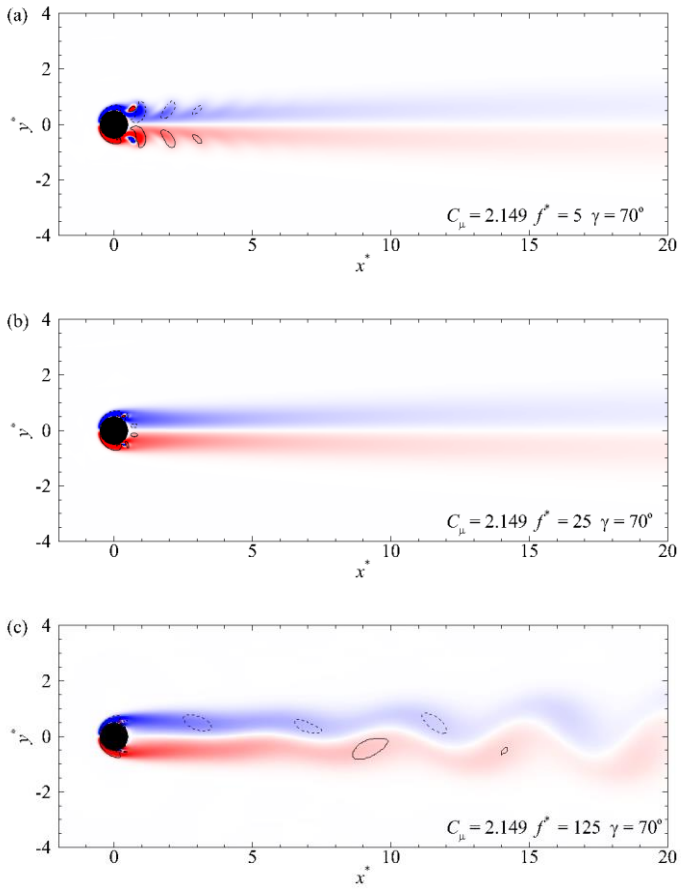

Fig. 13. Wake patterns for (a) γ = 70°, C_μ = 2.149, f^* = 5; (b) γ = 70°, C_μ = 2.149, f^* = 25; (c) γ = 70°, C_μ = 2.149, f^* = 125. The contour is normalized vorticity ω^*. The solid and dash lines represent vortices identified by λ_{ci} = 0.2 isolines enclosing positive and negative vorticity, respectively. Refer to Fig. 5(a) for the colorbar.

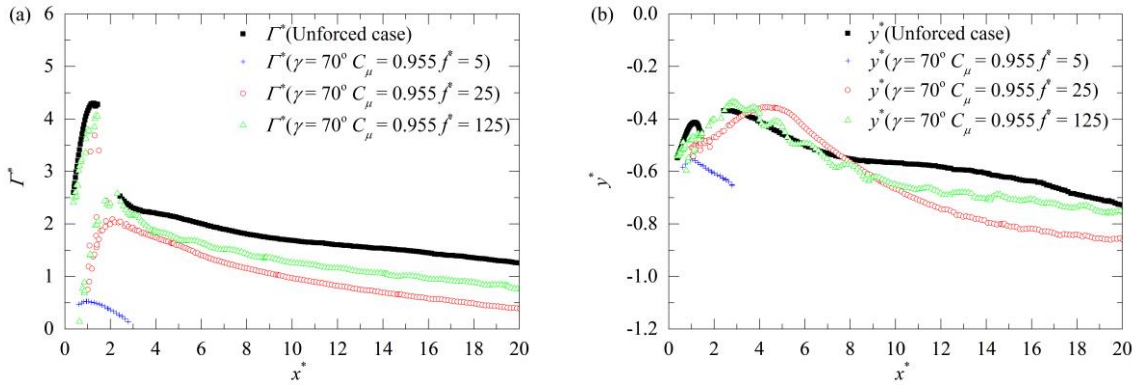

Fig. 14. Evolution of (a) normalized vortex circulation Γ^* and (b) normalized vortex position $y^* = y/D$ against streamwise position $x^* = x/D$. Symbols ■, +, ○, and Δ represent the unforced case; $\gamma = 70°$, $C_\mu = 0.955$, $f^* = 5$; $\gamma = 70°$, $C_\mu = 0.955$, $f^* = 25$; $\gamma = 70°$, $C_\mu = 0.955$, $f^* = 125$, respectively.

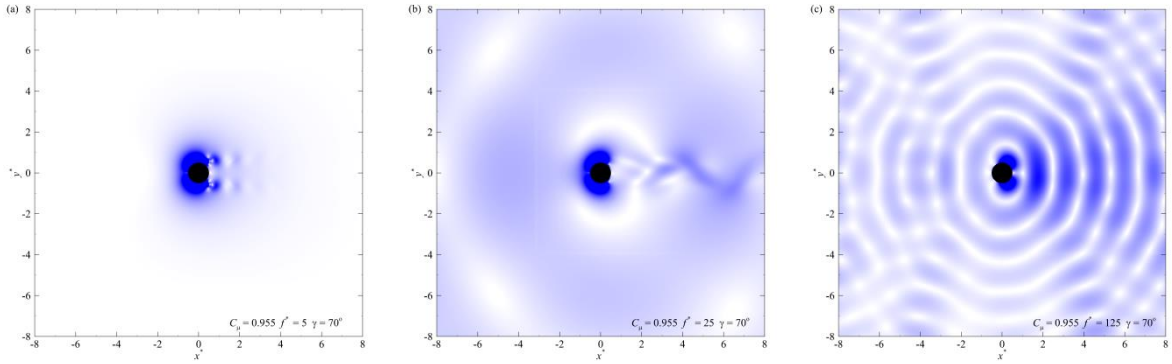

Fig. 15. Instantaneous pseudo-Schlieren visualization: γ = 70°, C_μ = 0.955, and (a) f^* = 5; (b) f^* = 25; (c) f^* = 125. For better presentation, the contour scale in (c) is 10 times of those in (a) and (b).

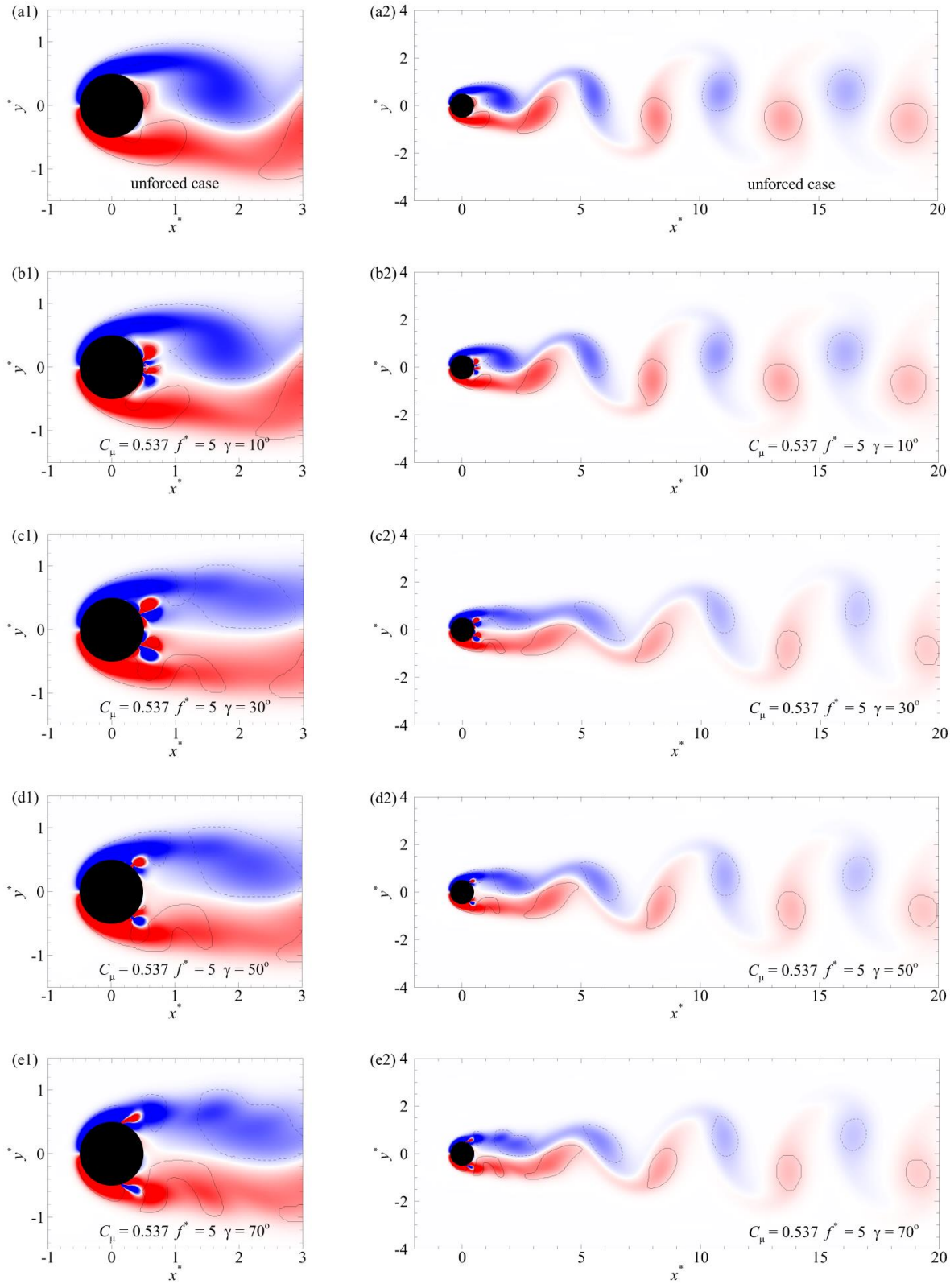
(a1)
unforced case
(a2)
unforced case
(b1)
$C_\mu = 0.537$ $f^* = 5$ $\gamma = 10^o$
(b2)
$C_\mu = 0.537$ $f^* = 5$ $\gamma = 10^o$
(c1)
$C_\mu = 0.537$ $f^* = 5$ $\gamma = 30^o$
(c2)
$C_\mu = 0.537$ $f^* = 5$ $\gamma = 30^o$
(d1)
$C_\mu = 0.537$ $f^* = 5$ $\gamma = 50^o$
(d2)
$C_\mu = 0.537$ $f^* = 5$ $\gamma = 50^o$
(e1)
$C_\mu = 0.537$ $f^* = 5$ $\gamma = 70^o$
(e2)
$C_\mu = 0.537$ $f^* = 5$ $\gamma = 70^o$
x^*
y^*

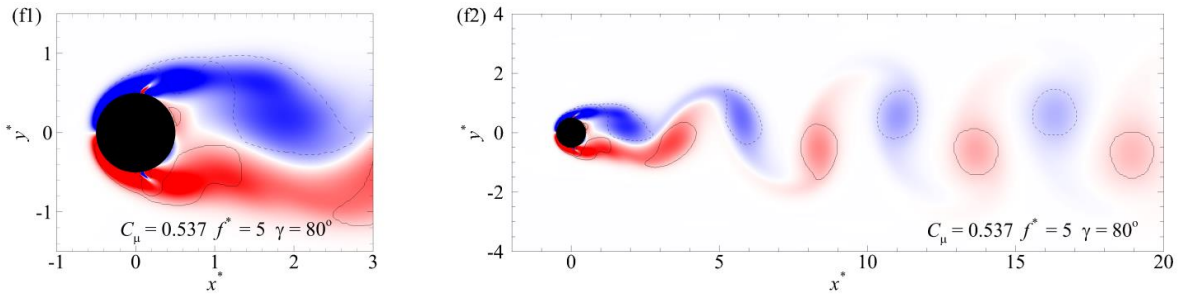

Fig. 16. Near and far field wake patterns: (a) unforced case; (b) C_μ = 0.537, f^* = 5, γ = 10°; (c) C_μ = 0.537, f^* = 5, γ = 30°; (d) C_μ = 0.537, f^* = 5, γ = 50°; (e) C_μ = 0.537, f^* = 5, γ = 70°; (f) C_μ = 0.537, f^* = 5, γ = 80°. The contour is normalized vorticity ω^*. The solid and dash lines represent vortices identified by λ_{ci} = 0.2 isolines enclosing positive and negative vorticity, respectively. Refer to Fig. 5(a) for the colorbar.

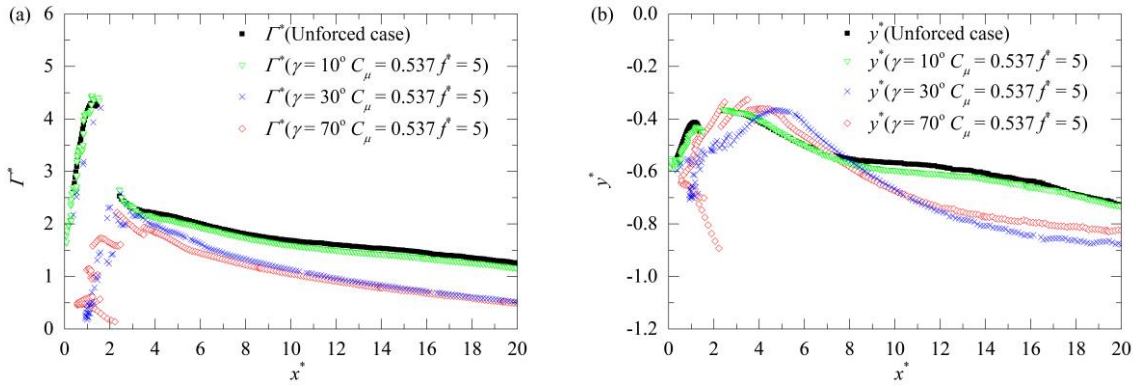

Fig. 17. Evolution of (a) normalized vortex circulation Γ^* and (b) normalized vortex position $y^* = y/D$ against streamwise position $x^* = x/D$. Symbols ■, ∇, × and ◇ represent the unforced case; $\gamma = 10°$, $C_\mu = 0.537$, $f^* = 5$; $\gamma = 30°$, $C_\mu = 0.537$, $f^* = 5$; $\gamma = 70°$, $C_\mu = 0.537$, $f^* = 5$, respectively.

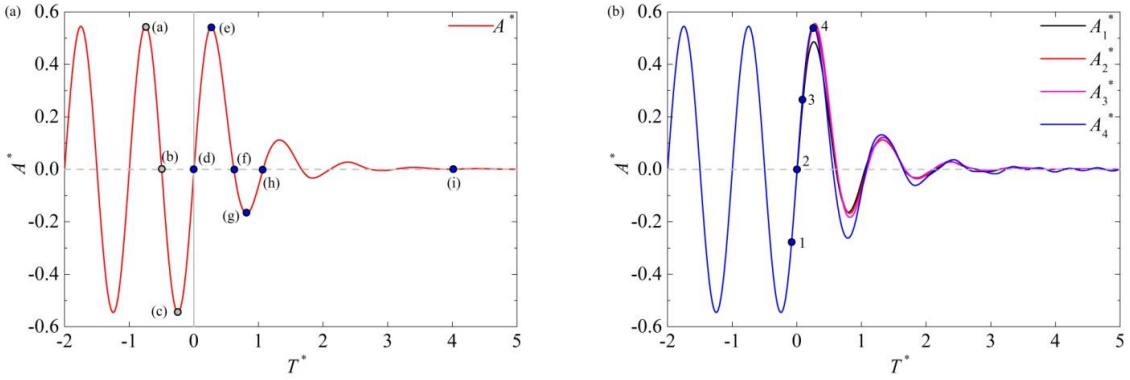

Fig. 18. Time history of the cross-flow position of the oscillating cylinder: (left) when the SJs are actuated at point (d); (right) when the SJs are actuated at points (1) to (4).

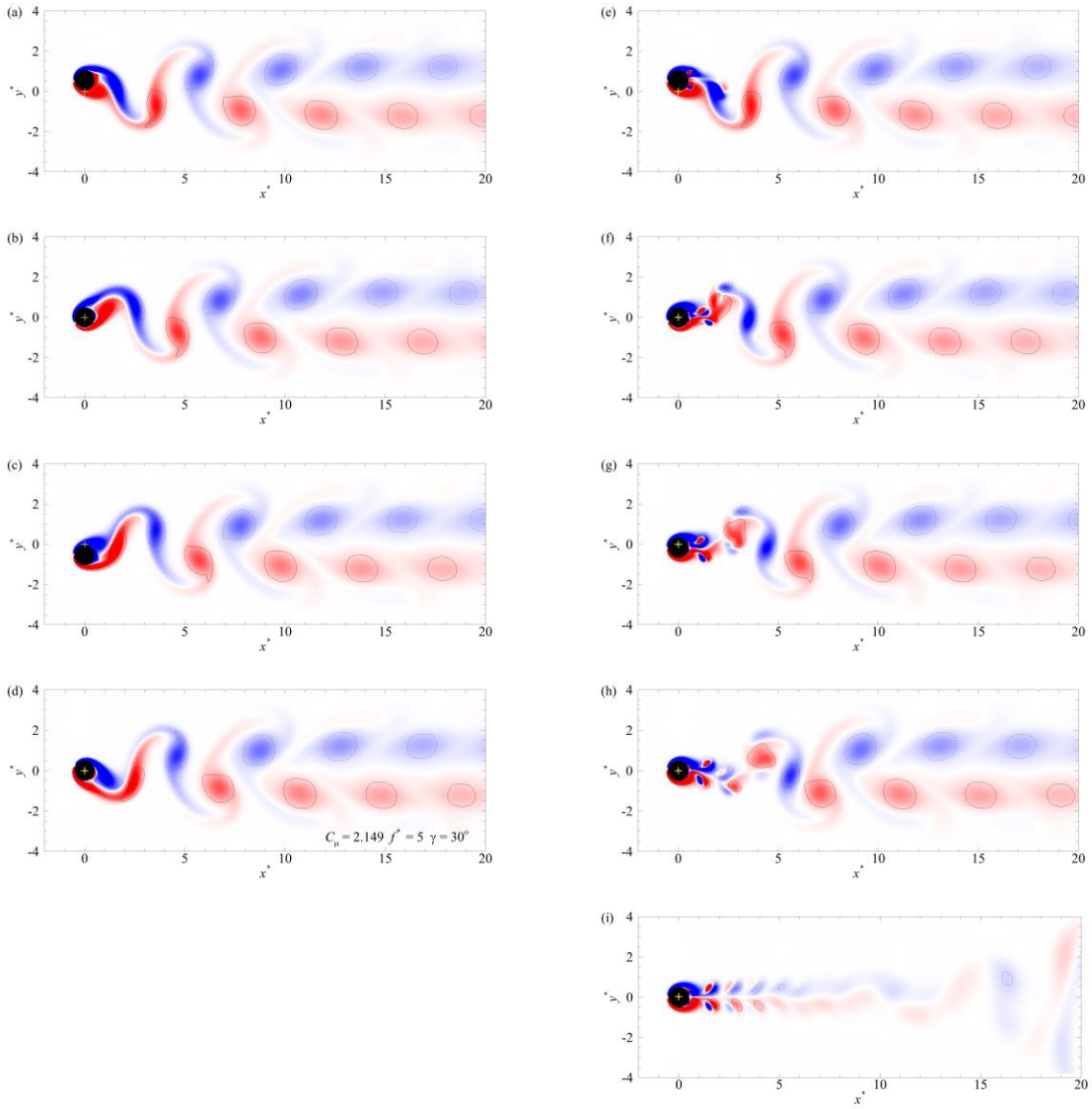

Fig. 19. Snapshots of cylinder position and wake patterns: (a) to (i) correspond to points (a) to (i) in Fig. 18 (a). The contour is normalized vorticity ω^*. The solid and dash lines represent vortices identified by λ_{ci} = 0.2 isolines enclosing positive and negative vorticity, respectively. Refer to Fig. 5(a) for the colorbar.